

A Cartesian Cut-Cell Two-Fluid Method for Two-Phase Diffusion Problems

Louis Libat ^{*1}, Can Selçuk¹, Eric Chénier¹, and Vincent Le Chenadec¹

¹MSME, Université Gustave Eiffel, UMR CNRS 8208, Marne-la-Vallée, 77454, France

January 7, 2026

Abstract

We present a Cartesian cut-cell finite-volume method for sharp-interface two-phase diffusion problems in static geometries. The formulation follows a two-fluid approach: independent diffusion equations are discretized in each phase on a fixed Cartesian grid, while the phases are coupled through embedded interface conditions enforcing continuity of diffusive flux and a general jump law. Cut cells are treated by integrating the governing equations over phase-restricted control volumes and surfaces, yielding discrete divergence and gradient operators that are locally conservative within each phase. Interface coupling is achieved by introducing a small set of interfacial unknowns per cut cell on the embedded boundary; the resulting algebraic system involves only bulk and interfacial averages. A key feature of the method is the use of a reduced set of geometric information based solely on low-order moments (trimmed volumes, apertures and interface measures/centroids), allowing robust implementation without constructing explicitly cut-cell polytopes. The method supports steady (Poisson) and unsteady (diffusion) regimes and incorporates Dirichlet, Neumann, Robin boundary conditions and general jumps. We validate the scheme on one-, two- and three-dimensional single-phase and two-phase benchmarks, including curved embedded boundaries, Robin conditions and strong property/jump contrasts. The results demonstrate a superlinear convergence behavior, sharp enforcement of interfacial laws and excellent conservation properties. Extensions to moving interfaces and Stefan-type free-boundary problems are natural perspectives of this framework.

1 Introduction

Diffusive transport across material interfaces is central to a wide range of heat- and mass-transfer phenomena, including conjugate heat transfer between solids and fluids, interphase species transfer, dissolution/precipitation in porous media and phase-change processes. At the continuum level, these problems are naturally formulated as two-phase diffusion models in which a scalar field (e.g. temperature or concentration) satisfies diffusion equations with phase-dependent coefficients and is coupled across a sharp interface through jump relations and flux balance [1, 7, 4, 12]. Depending on the application, the interface may enforce continuity of the scalar (conjugate heat transfer), a weighted jump such as Henry’s law (partitioning in mass transfer) or a finite interfacial resistance such as Kapitza resistance [26, 21]. These interfacial relations must be satisfied accurately to predict transfer rates, which are often limited by diffusive fluxes localized near the interface.

From a numerical standpoint, sharp-interface diffusion on complex geometries is challenging whenever the computational mesh does not conform to the interface. Body-fitted (ALE-type) approaches can represent the interface explicitly but require mesh generation and mesh motion, with the attendant complexity and robustness issues in three dimensions [10]. On fixed Cartesian grids, a broad class of non-conforming strategies has therefore been developed. Immersed-boundary and ghost/immersed-interface-type methods modify stencils near the interface or introduce forcing terms so that boundary and interface conditions are satisfied approximately, often with excellent accuracy for smooth solutions but with less direct control over strict local conservation [20, 9, 8, 31]. Interface-capturing methods (VOF or level-set approaches) [11, 19, 23] coupled with a one-fluid formulation offer flexibility for complex topological changes; however, enforcing two-phase diffusion jump conditions sharply on a fixed grid

^{*}Corresponding author: louis.libat2@univ-eiffel.fr

typically requires additional reconstruction and coupling machinery (and, in practice, often relies on one-fluid effective-property closures in interfacial cells). Hybrid combinations have recently been explored for solidification/melt problems [16] and XFEM/level-set formulations have also been used for coupled Stefan/mass-transport settings [15], highlighting continued interest in sharp and accurate interfacial transfer.

A particularly attractive class of methods for diffusion on Cartesian grids is the family of embedded-boundary (cut-cell) finite-volume schemes, which retain a conservative flux balance by trimming control volumes intersected by the interface. Seminal works include the embedded-boundary Poisson solver of [13], the Cartesian-grid advection-diffusion method of [3] and the three-dimensional heat/Poisson embedded-boundary method of [29]. These approaches demonstrate that cut-cell finite volumes can combine geometric flexibility with conservation and sharp boundary enforcement. Extensions and related developments have been pursued for higher-order finite-volume discretizations and locally refined grids [17], as well as for viscous incompressible flows in complex geometries on staggered meshes [30, 25]. Despite this progress, comparatively fewer works provide a two-fluid, conservative cut-cell formulation tailored to two-phase diffusion where the diffusion equations are solved independently in each phase and general jump laws are enforced sharply at the embedded interface, without resorting to smeared effective properties in mixed cells.

In this paper, we introduce a conservative Cartesian cut-cell finite-volume framework for two-phase diffusion problems in static geometries. The interface is fixed in time, while the scalar fields may be obey to a steady (Poisson) or unsteady diffusion equation. The method follows a two-fluid philosophy: each phase carries its own bulk unknowns and cut cells contain two phase-restricted control volumes. To enforce interfacial jump conditions in a sharp and locally conservative manner, we introduce, in addition to bulk cell averages, a small set of interfacial unknowns per cut cell representing interface averages. The discrete operators are derived by consistent application of Gauss' theorem on the trimmed volumes and faces, leading to conservative divergence and gradient operators whose interface contributions appear only through geometric weights and local coupling terms.

A key design goal is practical robustness: rather than explicitly constructing trimmed polytopes for every intersection pattern, the method is written entirely in terms of a reduced set of geometric moments (phase volumes, face apertures, interface measures and centroids). These moments can be computed using dedicated quadrature methods for implicitly defined interfaces [28], VOF-type geometric tools [6], or general-purpose geometry engines in two dimensions [27]. This moment-based viewpoint keeps the algebraic structure of the discretization independent of the geometric complexity, while preserving strict finite-volume conservation.

The main contributions of this work are:

- a conservative two-fluid cut-cell finite-volume discretization for steady and unsteady diffusion with phase-dependent coefficients and general sharp jump laws at an embedded interface;
- a unified enforcement mechanism for Dirichlet, Neumann and Robin conditions as well as weighted flux and scalar jumps that relies only on local geometric moments and nearest-neighbor couplings;
- a validation on one-, two- and three-dimensional benchmarks, mono- and two-phase, demonstrating a super-linear accuracy behavior together with conservation properties at the discrete level.

The paper is organized as follows. Sec. 2 introduces the two-phase continuum model and the interfacial jump conditions considered. Sec. 3 presents the embedded-boundary geometric setting and the reduced moment description used throughout. Sec. 4 derives the cut-cell finite-volume operators and the coupled discrete system. Numerical results are then reported in Sec. 5 to assess accuracy, robustness and conservation and Sec. 6 concludes and outlines extensions.

2 Continuum modeling

Transfers between two immiscible phases are considered in an open domain $\Omega \subset \mathbb{R}^d$ ($d \in \{1, 2, 3\}$). The domain Ω is partitioned into three subsets, a representative configuration of which is depicted in Fig. 1: the first two correspond to the physical regions occupied by the light, Ω^- and dark, Ω^+ , phases, while the last, Γ , corresponds to the sharp interface that separates the two phases. The immiscibility condition then reads,

$$\Omega^- \cap \Omega^+ = \emptyset. \quad (1)$$

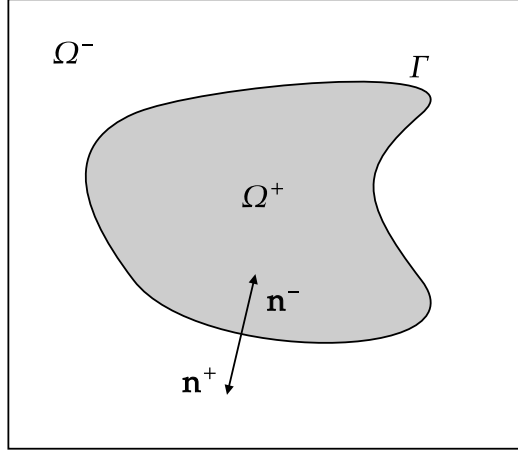


Figure 1: Fixed domain Ω with interface Γ , partitioning into Ω^- and Ω^+ . Normals \mathbf{n}^\pm point out of their respective phases.

and the saturation condition,

$$\Omega^- \cup \Gamma \cup \Omega^+ = \Omega. \quad (2)$$

The superscripts “ $-$ ” and “ $+$ ” denote quantities in the light and dark phases, respectively and \mathbf{n}^\pm are the unit normals on Γ pointing out of Ω^\pm . We choose the light phase as reference and set $\mathbf{n} := \mathbf{n}^-$, so that interfacial operators are defined with respect to \mathbf{n} . We employ the symbol $:=$ to mean “is defined as”.

We introduce a generic scalar field ϕ (e.g. temperature T or mass fraction x). The following describes the bulk transport model and the interfacial matching conditions used to close the two-phase diffusion problem.

2.1 Bulk transport equations

In each phase Ω^\pm , ϕ^\pm satisfies a balance equation of the form,

$$C^\pm \frac{\partial \phi^\pm}{\partial t} + \nabla \cdot \mathbf{q}^\pm = r^\pm \quad t > 0, \quad \mathbf{x} \in \Omega^\pm, \quad (3)$$

where the flux is assumed to be purely diffusive and closed by a constitutive equation such as Fourier’s or Fick’s law depending on whether the flow of heat or chemical species is considered,

$$\mathbf{q}^\pm := -K^\pm \nabla \phi^\pm, \quad (4)$$

where K^\pm is the diffusive mobility. The capacity C^\pm collects the storage term (e.g., $C^\pm = \rho^\pm c_p^\pm$ and $K^\pm = k^\pm$ for heat; $C^\pm = \rho^\pm$ and $K^\pm = D^\pm$ for species). In the context of this given article, the capacities C^\pm are assumed constant to maintain the linearity of the partial differential equations (PDEs). Variables capacities can also be treated but they introduce non-linearities which go beyond the scope or the current contribution. The symbol r^\pm represents any volumetric source or sink term.

The steady diffusion (Poisson) problem is recovered by neglecting transient storage effects, i.e. by setting $\partial_t \phi^\pm = 0$ in Eq. (3). In this case, the governing equations reduce to

$$\nabla \cdot \mathbf{q}^\pm = r^\pm, \quad \mathbf{x} \in \Omega^\pm, \quad (5)$$

supplemented by the same interfacial and boundary conditions as in the unsteady case.

2.2 Interfacial conditions

Let λ denote a scalar weight (typically constant) defined on the light domain ($\lambda: \Omega^- \rightarrow \mathbb{R}$). At any interfacial location $\mathbf{x} \in \Gamma$, we can then define the following weighted jump relative to the light phase,

$$[\![\phi]\!]^\lambda (t, \mathbf{x}) := \lim_{\epsilon \rightarrow 0^+} [\phi^+(t, \mathbf{x} - \epsilon \mathbf{n}^+) - (\lambda \phi^-)(t, \mathbf{x} - \epsilon \mathbf{n}^-)], \quad (6)$$

where \mathbf{n}^\pm are evaluated at \mathbf{x} . As will be noted below, the matching conditions used to close the equations will often fallback to the case where λ is identically one on Ω^- . Consequently, the following shorthand notation is introduced to denote the usual jump operator,

$$[\![\phi]\!] := [\![\phi]\!]^1.$$

The first type of interfacial condition arises from applying conservation principles at the interface. The conservation principle applied to the surface states that for ϕ to be conserved (and in the absence of line fluxes, surface accumulation and/or source/sink [12]), the fluxes normal to the interface cancel out and this reads,

$$[\![\mathbf{q} \cdot \mathbf{n}]\!](t, \mathbf{x}) = 0, \quad t > 0, \quad \mathbf{x} \in \Gamma, \quad (7)$$

In the case of conjugate heat transfer, Eq. (7) corresponds to continuity of the normal heat flux.

The balance equation Eq. (7) is not sufficient to close the problem Eq. (3). The flux balance (7) must be complemented by one additional interfacial relation. In the context of conjugate heat transfer, for example, the jump of the dependent variable is typically imposed,

$$[\![\phi]\!](t, \mathbf{x}) = f, \quad t > 0, \quad \mathbf{x} \in \Gamma, \quad (8)$$

whereas in conjugate mass transfer the concentration on either side may be related by Henry's law,

$$[\![\phi]\!]^{\text{He}}(t, \mathbf{x}) = f, \quad t > 0, \quad \mathbf{x} \in \Gamma \quad (9)$$

where He represents Henry's law constant, which tends to $\text{He} \rightarrow 1$ when the solubilities match across the interface [7, 26]. Also note that both Eqs. (8)-(9) include discontinuities (non-zero right-hand side f) to accommodate source terms [21].

The proposed framework can also accommodate more complex boundary conditions, such as nonlinearities (rate laws encountered in heterogeneous kinetics) and mixed boundary conditions (e.g. reservoir models with effective transfer coefficients). These extensions are not discussed here for brevity. As highlighted below, this is possible because the intrinsic diffusion equations on each domain are solved simultaneously, as opposed to a single transport equation for an effective fluid that occupies the union of both domains as in the one-fluid approach. This alleviates the modeling issue of effective properties in interfacial cells and enables the use of different models in each phase (convection, diffusion models...).

3 Discrete geometric representation

The continuum models introduced in Sec. 2 are discretized on a Cartesian grid. Focusing first on the representation of interfaces, this section introduces the discrete geometric quantities required by the cut-cell finite-volume operators.

A wide variety of techniques exist to represent interfaces. For simple objects (cuboids, cylinders, spheres, etc.), constructive solid geometry (CSG) is a convenient option [14]. More complex geometries can be approximated using simplicial meshes or splines (e.g. Bézier curves, NURBS) or described implicitly by a level-set function [19], in which a signed-distance field is either specified analytically or sampled on the background mesh and interpolated between nodes. The choice of interface representation is closely tied to the numerical strategy used to solve the surrounding fields. The Arbitrary Lagrangian–Eulerian (ALE) formulation, for instance, is well suited when the interface is discretized with segments (in $d = 2$) or triangles (in $d = 3$) but it requires moving unstructured meshes. On fixed structured meshes (predominantly Cartesian), the flows on either side of the interface can instead be computed using the cut-cell method, a finite-volume approach typically classified as an embedded boundary method. This technique has been applied to the solution of the incompressible (single-phase) Navier–Stokes equations in complex geometries on staggered meshes, first by Veldman & Verstappen [30] and later by Botella [5]. In both cases, control volumes are explicitly constructed by determining the intersection of the interface with the Cartesian mesh. Once this construction is performed, differentiation operators are derived using the finite-volume methodology.

A major practical difficulty of explicit cut-cell constructions is the large number of topologically distinct intersection patterns. In a d -dimensional Cartesian cell (a hyperrectangle), the interface can in principle generate 2^{2^d} distinct in/out sign configurations at the 2^d vertices. For $d = 3$, this already yields 256 cases. Adding time as a fourth dimension yields a 4D hyperrectangle with $2^4 = 16$ vertices and $2^{2^4} = 65536$ possible sign configurations. Although symmetries can be exploited to reduce this number, the resulting independent cases are still considerable.

For this reason, the proposed method does not rely on an explicit construction of trimmed polyhedra. Instead, it relies on Green-Gauss theorem and quadrature rules to derive the discrete operators. These quadrature rules require only a reduced set of geometric moments, described in Sec. 3.2. The computation of these moments thus constitutes the main bottleneck of the proposed method. It can be carried out with a handful of computational-geometry techniques and libraries. As shown below, this algorithmic choice is facilitated by the fact that all required moments reduce to intersections of hyperrectangles with the light (or dark) domain. For this purpose, efficient algorithms exist. For implicitly defined geometries, Saye's high-order quadrature methods provide accurate surface/volume integration directly from a level-set description [28]. The VOFI library also offers high-precision volume-of-fluid integration and related geometric quantities for implicitly defined interfaces [6]. In two dimensions, general-purpose geometry engines such as GEOS/LibGEOS provide robust polygon operations (intersection, area, centroid) [27], which can be useful for handling complex planar geometries. Altogether, such tools substantially simplify the implementation of the proposed method.

3.1 Geometrical foundations

We now introduce all of geometric quantities required to assemble the discrete operators in Sec. 4. For the sake of brevity, this section focuses on the two-dimensional case ($d = 2$). Three-dimensional extension can readily be performed.

Let $X := (x_{1/2}, x_{3/2}, \dots, x_{N+1/2}) \in \mathbb{R}^{N+1}$ ($N \in \mathbb{N}^*$) and $Y := (y_{1/2}, y_{3/2}, \dots, y_{M+1/2}) \in \mathbb{R}^{M+1}$ ($M \in \mathbb{N}^*$) denote two vectors of strictly increasing abscissas,

$$x_{1/2} < x_{3/2} < \dots < x_{N+1/2} \quad \text{and} \quad y_{1/2} < y_{3/2} < \dots < y_{M+1/2}.$$

We also define the following notation,

$$\Delta_i^1 :=]x_{i-1/2}, x_{i+1/2}[\quad \text{and} \quad \Delta_j^2 :=]y_{j-1/2}, y_{j+1/2}[,$$

where the superscripts indicate the directions and where

$$]a, b[:= \{\xi \in \mathbb{R} \text{ s.t. } a < \xi < b\}, \quad (a, b) \in \mathbb{R}^2$$

denotes a finite open interval.

The rectilinear mesh is defined using the Cartesian product: in two spatial dimensions,

$$\Omega_{i,j} := \Delta_i^1 \times \Delta_j^2, \quad (i, j) \in [1 \dots N] \times [1 \dots M]$$

where,

$$[m \dots n] := \{i \in \mathbb{Z} \text{ s.t. } m \leq i \leq n\}, \quad (m, n) \in \mathbb{Z}^2$$

denotes a set of consecutive integers.

To describe the intrinsic properties of each phase, the intersection of the mesh cells with each phase's domain is introduced as follows: let,

$$\Omega_{i,j}^\pm := \Omega_{i,j} \cap \Omega^\pm \tag{10}$$

denote the subset of $\Omega_{i,j}$ occupied by the light/dark phase and

$$\Gamma_{i,j} := \Omega_{i,j} \cap \Gamma$$

the subset of interface within $\Omega_{i,j}$. From the immiscibility condition Eq. (1), it follows that,

$$\Omega_{i,j} = \Omega_{i,j}^- \cup \Gamma_{i,j} \cup \Omega_{i,j}^+, \tag{11}$$

where all the subsets on the right-hand side are disjoint (See Fig 2b).

These notations enable the following definitions. A cell (i, j) is referred to as purely dark (resp., light) if $\Omega_{i,j}^+ = \Omega_{i,j}$ (resp., $\Omega_{i,j}^- = \Omega_{i,j}$). From the immiscibility condition, it follows that a purely dark cell is void of light medium (and vice versa). A cell (i, j) is said to be mixed if $\Gamma_{i,j} \neq \emptyset$.

We also introduce the notation,

$$\Omega_j^{1\pm}(\Delta) := (\Delta \times \Delta_j^2) \cap \Omega^\pm \quad \text{and} \quad \Omega_i^{2\pm}(\Delta) := (\Delta_i^1 \times \Delta) \cap \Omega^\pm$$

where Δ denotes a open interval. Note that, $\Omega_j^{1\pm}(\Delta)$ and $\Omega_i^{2\pm}(\Delta)$ are both subsets of \mathbb{R}^2 .

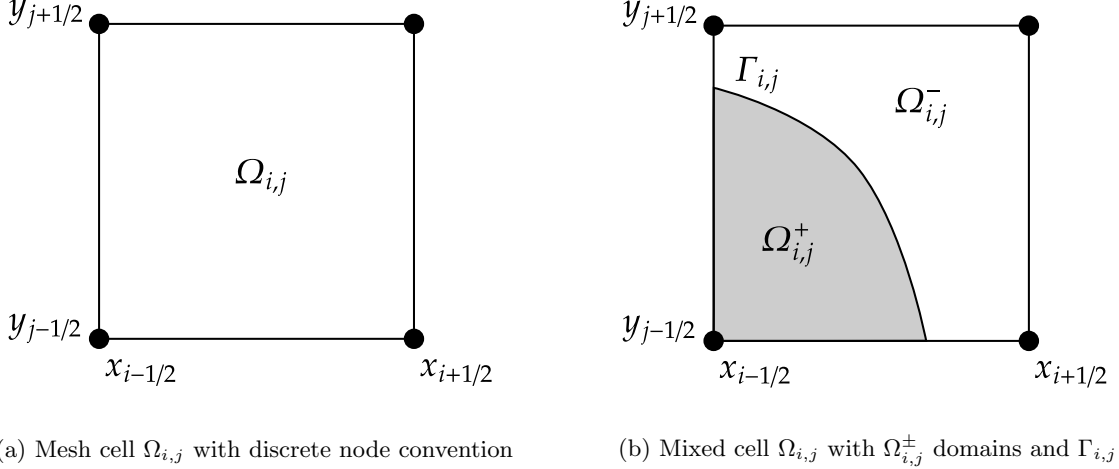


Figure 2: Mesh cell notations

As was previously done for the cells, the intersection of mesh faces with the phases' domains is also introduced as follows. Let

$$\Sigma_j^{1\pm}(x) := \{y \in \Delta_j^2 \text{ s.t. } (x, y) \in \Omega^{\pm}\}, \quad j \in [1 \dots M+1]$$

and

$$\Sigma_i^{2\pm}(y) := \{x \in \Delta_i^1 \text{ s.t. } (x, y) \in \Omega^{\pm}\}, \quad i \in [1 \dots N+1].$$

Note that for all $(x, y) \in \mathbb{R}^2$, $\Sigma_j^{1\pm}(x)$ and $\Sigma_i^{2\pm}(y)$ are both subsets of \mathbb{R} .

The description is completed by defining the corresponding faces in \mathbb{R}^2 , that is defining both,

$$\Sigma_{i-1/2,j}^{1\pm} := \{(x, y) \in \{x_{i-1/2}\} \times \Delta_j^2 \text{ s.t. } (x, y) \in \Omega^{\pm}\},$$

and,

$$\Sigma_{i,j-1/2}^{2\pm} := \{(x, y) \in \Delta_i^1 \times \{y_{j-1/2}\} \text{ s.t. } (x, y) \in \Omega^{\pm}\},$$

The qualifiers employed earlier for the cells (pure and mixed) also apply to these faces. Finally, the subsets thus defined realize a partition of the boundary (vertices excluded) of each phase (See Fig 3),

$$\partial\Omega_{i,j}^{\pm} \simeq \Gamma_{i,j} \cup \Sigma_{i-1/2,j}^{1\pm} \cup \Sigma_{i+1/2,j}^{1\pm} \cup \Sigma_{i,j-1/2}^{2\pm} \cup \Sigma_{i,j+1/2}^{2\pm}. \quad (12)$$

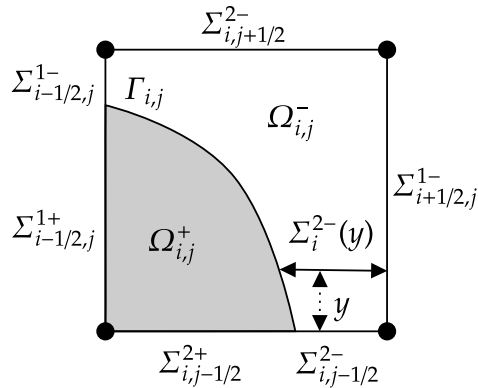


Figure 3: Mesh cell $\Omega_{i,j}$ with interface $\Gamma_{i,j}$ separating dark $\Omega_{i,j}^{+}$ and light regions $\Omega_{i,j}^{-}$. Intersections of mesh faces with phases' domains is also represented

3.2 Reduced geometric description

Let Ξ denote a subset of \mathbb{R}^d ($d \in \mathbb{N}^*$) and f a function defined over Ξ (f is typically a monomial, as shown below). We denote the integral of f over Ξ with the following shorthand notation,

$$\langle \Xi, f \rangle := \int_{(x_1 \dots x_d) \in \Xi} f(x_1, \dots, x_d) \, dx_1 \dots dx_d \quad (13)$$

which will be employed over cells, faces and interface segments. (Here x_1, \dots, x_d denote Cartesian coordinates).

In the computer-graphics literature these same quantities are often called geometric moments [18]. These same moments are employed in various cut-cell discretizations to compute irregular cell volumes and face apertures needed for flux evaluation [24]. We also note that the notation introduced in Eq. (13) is sufficient, since all required geometric information is expressed as integrals over the intersection of hyperrectangles with phase domains.

3.2.1 Primary geometric moments

As mentioned above, only low-order moments are required to assemble the discrete operators. This section therefore introduces shorthand notations for such moments. Let us first denote the volumes,

$$V_{i,j} := \langle \Omega_{i,j}, 1 \rangle = (x_{i+1/2} - x_{i-1/2}) (y_{j+1/2} - y_{j-1/2})$$

and

$$V_{i,j}^\pm := \langle \Omega_{i,j}^\pm, 1 \rangle. \quad (14)$$

The centroids along x are defined as (See Fig 4),

$$x_i := \frac{\langle \Omega_{i,j}, x \rangle}{\langle \Omega_{i,j}, 1 \rangle} = \frac{x_{i-1/2} + x_{i+1/2}}{2}$$

and

$$x_{i,j}^\pm := \begin{cases} \langle \Omega_{i,j}^\pm, x \rangle / \langle \Omega_{i,j}^\pm, 1 \rangle, & \text{if } \Omega_{i,j}^\pm \neq \emptyset, \\ x_i, & \text{otherwise.} \end{cases} \quad (15)$$

Likewise,

$$y_j := \frac{\langle \Omega_{i,j}, y \rangle}{\langle \Omega_{i,j}, 1 \rangle} \left(= \frac{y_{j-1/2} + y_{j+1/2}}{2} \right)$$

and

$$y_{i,j}^\pm := \begin{cases} \langle \Omega_{i,j}^\pm, y \rangle / \langle \Omega_{i,j}^\pm, 1 \rangle, & \text{if } \Omega_{i,j}^\pm \neq \emptyset, \\ y_j, & \text{otherwise.} \end{cases} \quad (16)$$

The definitions Eq. (15) and Eq. (16) remain valid for empty cells, for which either $V_{i,j}^+$ or $V_{i,j}^-$ vanishes. In such instances, this enables a consistent definitions of the secondary geometric moments, defined in the next section.

This construction also guarantees that the centroids lie within the convex hull of the $\Omega_{i,j}$, i.e.

$$x_{i-1/2} \leq x_{i,j}^\pm \leq x_{i+1/2}, \quad y_{j-1/2} \leq y_{i,j}^\pm \leq y_{j+1/2}. \quad (17)$$

We also introduce the following face-centered quantity (See Fig 5),

$$A_{i-1/2,j}^{1\pm} := \langle \Sigma_{i-1/2,j}^{1\pm}, 1 \rangle, \quad A_{i,j-1/2}^{2\pm} := \langle \Sigma_{i,j-1/2}^{2\pm}, 1 \rangle. \quad (18)$$

Using both the rectilinearity of the grid and the saturation and immiscibility conditions Eqs. (1) and (2),

$$\begin{aligned} V_{i,j} &= V_{i,j}^- + V_{i,j}^+, \\ x_i V_{i,j} &= x_{i,j}^- V_{i,j}^- + x_{i,j}^+ V_{i,j}^+ \quad \text{and} \quad y_j V_{i,j} = y_{i,j}^- V_{i,j}^- + y_{i,j}^+ V_{i,j}^+ \end{aligned}$$

and finally,

$$A_j^1 = A_{i-1/2,j}^{1-} + A_{i-1/2,j}^{1+} \quad \text{and} \quad A_i^2 = A_{i,j-1/2}^{2-} + A_{i,j-1/2}^{2+}.$$

where $A_j^1 := y_{j+1/2} - y_{j-1/2}$ and $A_i^2 := x_{i+1/2} - x_{i-1/2}$.

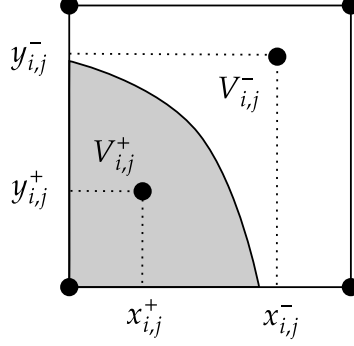


Figure 4: Cut cell with the domains $\Omega_{i,j}^+$ (dark) and $\Omega_{i,j}^-$ (light), with bulk centroids $(x_{i,j}^\pm, y_{i,j}^\pm)$ and their associated $V_{i,j}^\pm$

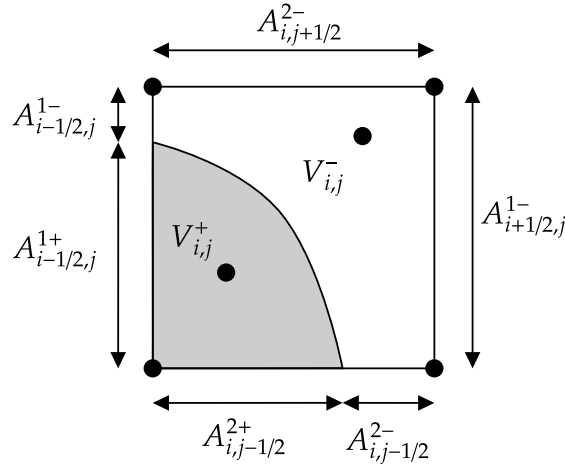


Figure 5: Cut cell $\Omega_{i,j}$ with the domains $\Omega_{i,j}^+$ (dark) and $\Omega_{i,j}^-$ (light), with face-areas $A_{i\pm\frac{1}{2},j}^{1\pm}$, $A_{i,j\pm\frac{1}{2}}^{2\pm}$.

3.2.2 Secondary geometric moments

The geometric moments defined below are referred to as “secondary” simply because their definition depends on the previously introduced “primary geometric moment”.

We define the following cell-centered averages (See Fig 6),

$$B_{i,j}^{1\pm} := \langle \Sigma_j^{1\pm}(x_{i,j}^\pm), 1 \rangle, \quad B_{i,j}^{2\pm} := \langle \Sigma_i^{2\pm}(y_{i,j}^\pm), 1 \rangle. \quad (19)$$

Let us also define the x -face-centered volume as,

$$W_{i-1/2,j}^{1\pm} := \langle \Omega_j^{1\pm}([x_{i-1,j}^\pm, x_{i,j}^\pm]), 1 \rangle. \quad (20)$$

Using the linearity of the integral, the latter moment can also be computed as,

$$W_{i-1/2,j}^{1\pm} = \langle \Omega_j^{1\pm}([x_{i-1,j}^\pm, x_{i-1/2}]), 1 \rangle + \langle \Omega_j^{1\pm}([x_{i-1/2}, x_{i,j}^\pm]), 1 \rangle,$$

Using Eq. (17), we note that $x_{i-1,j}^\pm(t) < x_{i-1/2} < x_{i,j}^\pm(t)$ and hence the right-hand side is the sum of two positive quantities. Likewise, along y -aligned faces we define,

$$W_{i,j-1/2}^{2\pm} := \langle \Omega_i^{2\pm}([y_{i,j-1}^\pm, y_{i,j}^\pm]), 1 \rangle,$$

which can also be rewritten as the sum of two positive quantities as done in Eq. (20).

A summary table, located in the appendix 10, summarizes, for two spatial dimensions, the geometric moments used in the discrete formulation.

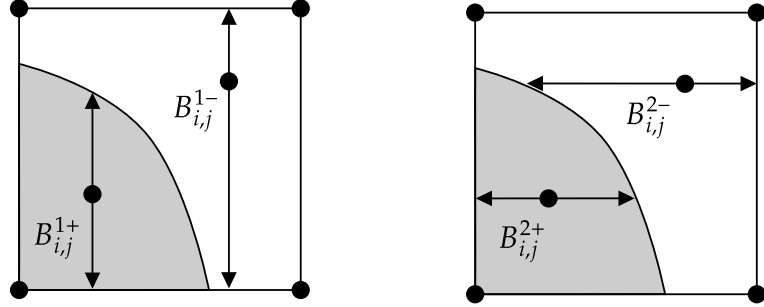


Figure 6: Cut cell $\Omega_{i,j}$ with the domains $\Omega_{i,j}^+$ (dark) and $\Omega_{i,j}^-$ (light), with centroid-areas $B_{i,j}^{1\pm}$, $B_{i,j}^{2\pm}$

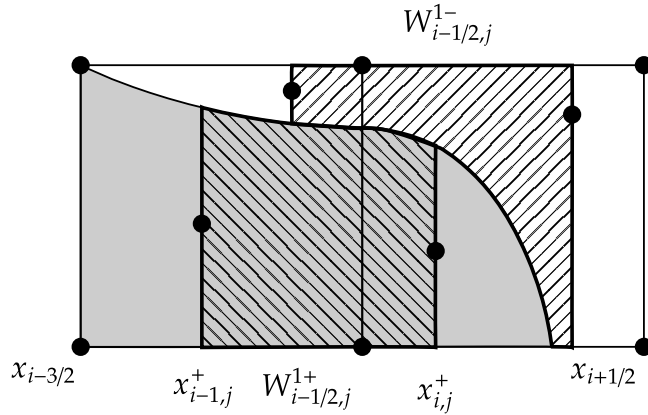


Figure 7: Two adjacent cut cells. The right striped region $W_{i-\frac{1}{2},j}^{1-}$ and the left striped region $W_{i-\frac{1}{2},j}^{1+}$ are shown in the cells.

4 Two-phase cut-cell method for static domains

We now turn our attention to the discretization of the two scalar transport equations Eq. (3) on fixed subdomains i.e. Ω^\pm . The formulation is based on the single-phase cut-cell method developed in [25]. The novelty here lies in its extension to two-phase diffusion with interfacial matching conditions. This extension proceeds as follows: bulk and interfacial variables are introduced in each domain, with the exact number of unknowns depending on the interface topology and the Cartesian mesh. The key question then becomes how to impose discrete constraints that uniquely determine these unknowns.

Let us introduce a sequence of strictly increasing time instants,

$$t_0 < t_1 < \dots < t_n < \dots$$

where t_0 is set to 0, consistently with the continuum model (See Sec. 2)

For each mixed cells, the semi-discrete interfacial variables are defined as,

$$\Phi_{i,j}^{\gamma\pm}(t) := \frac{\int_{\Gamma_{i,j}} \phi^\pm(t, \mathbf{x}) \, dS}{\int_{\Gamma_{i,j}} dS},$$

and their discrete-in-time counterparts

$$\Phi_{n,i,j}^{\gamma\pm} := \Phi_{i,j}^{\gamma\pm}(t_n). \quad (21)$$

These interfacial unknowns are associated with the two interface conditions (Eqs. (7)-(8) or Eqs. (7)-(9) depending on the the problem at hand).

In each active cell, we define the semi-discrete bulk variables as,

$$\Phi_{i,j}^{\omega\pm}(t) := \langle \Omega_{i,j}^\pm, \phi^\pm(t) \rangle / V_{i,j}^\pm \quad \text{where} \quad V_{i,j}^\pm \neq 0,$$

and the discrete bulk variables as,

$$\Phi_{n,i,j}^{\omega\pm} := \Phi_{i,j}^{\omega\pm}(t_n). \quad (22)$$

They are associated with the semi-discrete and discrete bulk equations, respectively.

4.1 Semi-discrete bulk equations

As for the primary variables, we represent the Cartesian components of the flux \mathbf{q}^\pm by face averages. Let $q^{1\pm} := \mathbf{q}^\pm \cdot \mathbf{e}^1$ and $q^{2\pm} := \mathbf{q}^\pm \cdot \mathbf{e}^2$, where \mathbf{e}^α denotes the α -th Cartesian basis vector. On vertical faces, we define

$$Q_{i-1/2,j}^{1\pm}(t) := \frac{1}{A_{i-1/2,j}^{1\pm}} \int_{\Sigma_{i-1/2,j}^{1\pm}} q^{1\pm}(t, \mathbf{x}) \, dS, \quad \text{for } A_{i-1/2,j}^{1\pm} \neq 0, \quad (23)$$

and similarly on horizontal faces,

$$Q_{i,j-1/2}^{2\pm}(t) := \frac{1}{A_{i,j-1/2}^{2\pm}} \int_{\Sigma_{i,j-1/2}^{2\pm}} q^{2\pm}(t, \mathbf{x}) \, dS, \quad \text{for } A_{i,j-1/2}^{2\pm} \neq 0. \quad (24)$$

Integrating Eq. (3) over $\Omega_{i,j}^\pm$ and using the (divergence) Gauss theorem yields the semi-discrete balance

$$V_{i,j}^\pm C^\pm \frac{d\Phi_{i,j}^{\omega\pm}}{dt} + \int_{\partial\Omega_{i,j}^\pm} \mathbf{q}^\pm(t, \mathbf{x}) \cdot \mathbf{n}^\pm \, dS = \int_{\Omega_{i,j}^\pm} r^\pm(t, \mathbf{x}) \, dV. \quad (25)$$

4.1.1 Volume-integrated divergence operator

Using the partition Eq. (12), we split the boundary integral into its mesh-face and interface contributions:

$$\int_{\partial\Omega_{i,j}^\pm} \mathbf{q}^\pm \cdot \mathbf{n}^\pm \, dS = \int_{\partial\Omega_{i,j}^\pm \setminus \Gamma_{i,j}} \mathbf{q}^\pm \cdot \mathbf{n}^\pm \, dS + \int_{\Gamma_{i,j}} \mathbf{q}^\pm \cdot \mathbf{n}^\pm \, dS. \quad (26)$$

On mesh-aligned faces, the outward normals are $\pm\mathbf{e}^1$ and $\pm\mathbf{e}^2$, so that the first term can be written in conservative flux-difference form:

$$\begin{aligned} \int_{\partial\Omega_{i,j}^\pm \setminus \Gamma_{i,j}} \mathbf{q}^\pm \cdot \mathbf{n}^\pm \, dS &= A_{i+1/2,j}^{1\pm} Q_{i+1/2,j}^{1\pm}(t) - A_{i-1/2,j}^{1\pm} Q_{i-1/2,j}^{1\pm}(t) \\ &\quad + A_{i,j+1/2}^{2\pm} Q_{i,j+1/2}^{2\pm}(t) - A_{i,j-1/2}^{2\pm} Q_{i,j-1/2}^{2\pm}(t). \end{aligned} \quad (27)$$

We introduce directional (volume-integrated) divergence operators acting on generic apertures A and face fluxes Q :

$$\begin{cases} V_{i,j}^\pm \operatorname{div}_{i,j}^{1\omega}(A, Q) := A_{i+1/2,j} Q_{i+1/2,j} - A_{i-1/2,j} Q_{i-1/2,j}, \\ V_{i,j}^\pm \operatorname{div}_{i,j}^{2\omega}(A, Q) := A_{i,j+1/2} Q_{i,j+1/2} - A_{i,j-1/2} Q_{i,j-1/2}. \end{cases} \quad (28)$$

This step is the foundation of the finite-volume method: each contribution is an exchange through a well-identified boundary portion. By construction, internal exchanges cancel under telescopic summation, leaving only net boundary fluxes, thus ensuring global conservation within each phase.

The last term in Eq. (26), representing interfacial exchange, must be approximated using the available reduced geometric information. The discrete formula is designed to satisfy the following requirements: (i) minimal stencil, (ii) exact cancellation when the face fluxes are constant, (iii) at least first-order accuracy for mesh-aligned planar interfaces and (iv) recovery of the classical divergence away from interfaces.

We adopt the following approximation:

$$\begin{aligned} \int_{\Gamma_{i,j}} \mathbf{q}^\pm(t, \mathbf{x}) \cdot \mathbf{n}^\pm \, dS &\simeq (B_{i,j}^{1\pm} - A_{i+1/2,j}^{1\pm}) Q_{i+1/2,j}^{1\pm}(t) + (A_{i-1/2,j}^{1\pm} - B_{i,j}^{1\pm}) Q_{i-1/2,j}^{1\pm}(t) \\ &\quad + (B_{i,j}^{2\pm} - A_{i,j+1/2}^{2\pm}) Q_{i,j+1/2}^{2\pm}(t) + (A_{i,j-1/2}^{2\pm} - B_{i,j}^{2\pm}) Q_{i,j-1/2}^{2\pm}(t). \end{aligned} \quad (29)$$

We formalize this by introducing

$$\begin{cases} V_{i,j}^\pm \operatorname{div}_{i,j}^{1\gamma}(A, B, Q) := (B_{i,j} - A_{i+1/2,j}) Q_{i+1/2,j} + (A_{i-1/2,j} - B_{i,j}) Q_{i-1/2,j}, \\ V_{i,j}^\pm \operatorname{div}_{i,j}^{2\gamma}(A, B, Q) := (B_{i,j} - A_{i,j+1/2}) Q_{i,j+1/2} + (A_{i,j-1/2} - B_{i,j}) Q_{i,j-1/2}. \end{cases} \quad (30)$$

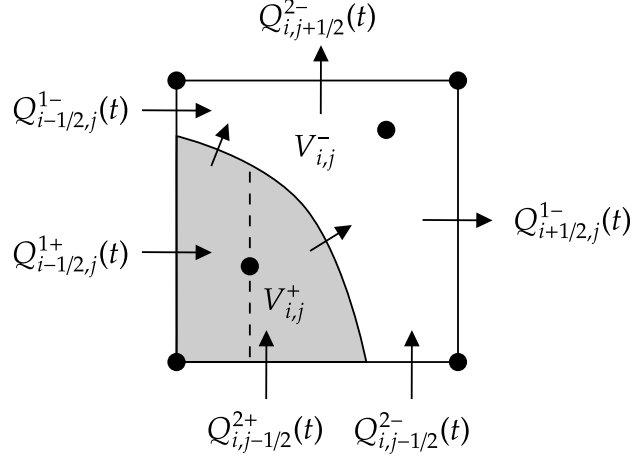


Figure 8: Schematic of the cut-cell divergence balance.

Summing the bulk (ω) and interfacial (γ) contributions Eq. (27) and Eq. (29), the terms proportional to $A^{\alpha\pm}$ cancel and the divergence can be expressed using $B^{\alpha\pm}$ only:

$$\begin{cases} V_{i,j}^\pm \operatorname{div}_{i,j}^1(B, Q) := B_{i,j} (Q_{i+1/2,j} - Q_{i-1/2,j}), \\ V_{i,j}^\pm \operatorname{div}_{i,j}^2(B, Q) := B_{i,j} (Q_{i,j+1/2} - Q_{i,j-1/2}). \end{cases}$$

As previously noted, an explicit construction of trimmed control volumes is not required; the formulation only relies on reduced geometric moments.

4.1.2 Gradient operator

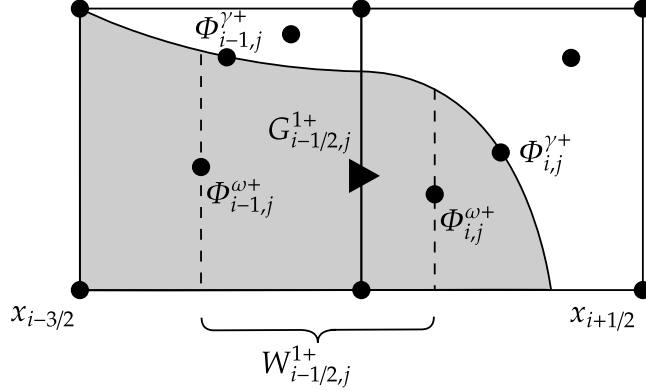


Figure 9: Schematic of the cut-cell gradient operator on the staggered volume $W_{i-\frac{1}{2},j}^{1+}$.

The first component of the gradient is represented by a staggered average

$$G_{i-1/2,j}^{1\pm}(t) := \frac{1}{W_{i-1/2,j}^{1\pm}} \langle \Omega_j^{1\pm}([x_{i-1,j}^\pm, x_{i,j}^\pm]), \partial_1 \phi^\pm(t, \cdot) \rangle, \quad \text{for } W_{i-1/2,j}^{1\pm} \neq 0, \quad (31)$$

where ∂_1 denotes the partial derivative with respect to x . Using the Gauss theorem on the staggered region and the linearity of the integral, we obtain

$$\begin{aligned} W_{i-1/2,j}^{1\pm} G_{i-1/2,j}^{1\pm}(t) &= \langle \Sigma_j^{1\pm}(x_{i,j}^\pm), \phi^\pm(t, \cdot) \rangle - \langle \Sigma_j^{1\pm}(x_{i-1,j}^\pm), \phi^\pm(t, \cdot) \rangle \\ &\quad + \int_{([x_{i-1,j}^\pm, x_{i,j}^\pm] \times \Delta_j^2) \cap \Gamma} \phi^\pm(t, \mathbf{x}) n^{1\pm}(\mathbf{x}) dS, \end{aligned} \quad (32)$$

where $n^{1\pm}$ is the first Cartesian component of the unit normal to Γ pointing out of Ω^\pm .

The two mesh-face terms are approximated by

$$\langle \Sigma_j^{1\pm}(x_{i,j}^\pm), \phi^\pm(t, \cdot) \rangle \simeq B_{i,j}^{1\pm} \Phi_{i,j}^{\omega\pm}(t), \quad \langle \Sigma_j^{1\pm}(x_{i-1,j}^\pm), \phi^\pm(t, \cdot) \rangle \simeq B_{i-1,j}^{1\pm} \Phi_{i-1,j}^{\omega\pm}(t), \quad (33)$$

which yields the bulk contribution

$$\text{grad}_{i-1/2,j}^{1\omega}(B, W, \Phi) := \frac{B_{i,j}\Phi_{i,j} - B_{i-1,j}\Phi_{i-1,j}}{W_{i-1/2,j}}.$$

The interfacial contribution (last term in Eq. (32)) is approximated by

$$\int_{([x_{i-1,j}^\pm, x_{i,j}^\pm] \times \Delta_j^2) \cap \Gamma} \phi^\pm(t, \mathbf{x}) n^{1\pm}(\mathbf{x}) dS \simeq (A_{i-1/2,j}^{1\pm} - B_{i,j}^{1\pm}) \Phi_{i,j}^{\gamma\pm}(t) - (A_{i-1/2,j}^{1\pm} - B_{i-1,j}^{1\pm}) \Phi_{i-1,j}^{\gamma\pm}(t), \quad (34)$$

leading to

$$\text{grad}_{i-1/2,j}^{1\gamma}(A, B, W, \Phi) := \frac{(A_{i-1/2,j} - B_{i,j})\Phi_{i,j} - (A_{i-1/2,j} - B_{i-1,j})\Phi_{i-1,j}}{W_{i-1/2,j}}.$$

The second component $G_{i,j-1/2}^{2\pm}(t)$ is constructed analogously on $W_{i,j-1/2}^{2\pm}$ using $B^{2\pm}$ and $A^{2\pm}$:

$$\begin{aligned} \text{grad}_{i,j-1/2}^{2\omega}(B, W, \Phi) &:= \frac{B_{i,j}\Phi_{i,j} - B_{i,j-1}\Phi_{i,j-1}}{W_{i,j-1/2}}, \\ \text{grad}_{i,j-1/2}^{2\gamma}(A, B, W, \Phi) &:= \frac{(A_{i,j-1/2} - B_{i,j})\Phi_{i,j} - (A_{i,j-1/2} - B_{i,j-1})\Phi_{i,j-1}}{W_{i,j-1/2}}. \end{aligned}$$

Finally, the constitutive relation Eq. (4) is imposed in discrete form by

$$Q_{i-1/2,j}^{1\pm}(t) \simeq -K^\pm G_{i-1/2,j}^{1\pm}(t), \quad Q_{i,j-1/2}^{2\pm}(t) \simeq -K^\pm G_{i,j-1/2}^{2\pm}(t),$$

where K^\pm is constant in each phase.

4.2 Semi-discrete interface conditions

The interfacial conservation law Eq. (7) corresponds to continuity of the diffusive flux,

$$[\![\mathbf{q} \cdot \mathbf{n}]\!] = 0 \quad \text{on } \Gamma.$$

Integrating over each local interface segment $\Gamma_{i,j}$ yields

$$\int_{\Gamma_{i,j}} [\![\mathbf{q} \cdot \mathbf{n}]\!] dS = 0. \quad (35)$$

The integrals in Eq. (35) correspond to the interfacial contributions appearing in the Gauss decomposition in Eq. (26). They are approximated using the discrete interfacial divergence operators $\text{div}^{\alpha\gamma}$ introduced in Eq. (30). Consequently, the flux balance is semi-discretized as

$$\sum_{\alpha=1}^d \left[V_{i,j}^+ \text{div}_{i,j}^{\alpha\gamma}(A^{\alpha+}, B^{\alpha+}, Q^{\alpha+}(t)) - V_{i,j}^- \text{div}_{i,j}^{\alpha\gamma}(A^{\alpha-}, B^{\alpha-}, Q^{\alpha-}(t)) \right] = 0. \quad (36)$$

For mixed cells (i, j) , the jump/closure condition in Eq. (8) (or in Eq. (9)) is semi-discretized as

$$\Phi_{i,j}^{\gamma+}(t) - \lambda \Phi_{i,j}^{\gamma-}(t) = F_{i,j}(t), \quad (37)$$

where

$$F_{i,j}(t) := \frac{\langle \Gamma_{i,j}, f(\cdot, t) \rangle}{\langle \Gamma_{i,j}, 1 \rangle} = \frac{\int_{\Gamma_{i,j}} f(\mathbf{x}, t) dS}{\int_{\Gamma_{i,j}} dS}.$$

and λ is the interfacial coefficient appearing in the weighted jump definition Eq. (6) (e.g. $\lambda = 1$ adn $f = 0$ to impose continuity of ϕ across the interface).

4.3 Discrete equations

We now use a θ -scheme time discretization of the semi-discrete bulk balances Eq. (25). For $0 \leq \theta \leq 1$, we approximate fluxes and sources at $t_{n+\theta} := (1 - \theta)t_n + \theta t_{n+1}$:

$$V_{i,j}^\pm C^\pm \frac{\Phi_{n+1,i,j}^{\omega\pm} - \Phi_{n,i,j}^{\omega\pm}}{\Delta t_n} + \sum_{\alpha=1}^d V_{i,j}^\pm \operatorname{div}_{i,j}^\alpha (B^{\alpha\pm}, Q_{n+\theta}^{\alpha\pm}) = V_{i,j}^\pm R_{n+\theta,i,j}^\pm, \quad (38)$$

where

$$R_{i,j}^\pm(t) := \frac{\langle \Omega_{i,j}^\pm, r^\pm(t, \cdot) \rangle}{V_{i,j}^\pm} = \frac{\int_{\Omega_{i,j}^\pm} r^\pm(t, \mathbf{x}) \, dV}{\int_{\Omega_{i,j}^\pm} dV},$$

and $\Delta t_n := t_{n+1} - t_n$. The choices $\theta = 0$ and $\theta = 1$ correspond to the forward and backward Euler schemes respectively and $\theta = \frac{1}{2}$ to the midpoint rule.

The bulk equations are closed by specifying the face fluxes using the discrete constitutive relation :

$$Q_{n+\theta}^{\alpha\pm} = -K^\pm \left[\operatorname{grad}^{\alpha\omega} (B^{\alpha\pm}, W^{\alpha\pm}, (1 - \theta)\Phi_n^{\omega\pm} + \theta\Phi_{n+1}^{\omega\pm}) + \operatorname{grad}^{\alpha\gamma} (A^{\alpha\pm}, B^{\alpha\pm}, W^{\alpha\pm}, \Phi_{n+\theta}^{\gamma\pm}) \right]. \quad (39)$$

For mixed cells, the interfacial flux balance is discretized consistently at $t_{n+\theta}$:

$$\sum_{\alpha=1}^d \left[V_{i,j}^+ \operatorname{div}_{i,j}^{\alpha\gamma} (A^{\alpha+}, B^{\alpha+}, Q_{n+\theta}^{\alpha+}) - V_{i,j}^- \operatorname{div}_{i,j}^{\alpha\gamma} (A^{\alpha-}, B^{\alpha-}, Q_{n+\theta}^{\alpha-}) \right] = 0. \quad (40)$$

Finally, the jump/closure condition is enforced at $t_{n+\theta}$ (where $\Phi_{n+\theta,i,j}^{\gamma\pm}$ are collocated):

$$\Phi_{n+\theta,i,j}^{\gamma+} - \lambda \Phi_{n+\theta,i,j}^{\gamma-} = F_{n+\theta,i,j}. \quad (41)$$

Choosing $\Phi^{\gamma\pm}$ at $t_{n+\theta}$ as primary unknowns (as opposed to t_n) avoids the need to explicitly extrapolate interfacial values when $\theta \neq 1$. Other time integration schemes may be employed, provided that bulk and interfacial conservation statements are discretized consistently.

4.4 Block structure of the linear system

Since the continuum model is linear, the corresponding discrete equations are linear and can be written in matrix-vector form. Even for $\theta = 0$ (forward Euler), the unknowns at time level $n + 1$ remain coupled through the interfacial conditions. The matrices are nevertheless sparse, as the discrete operators were designed to keep the stencil compact. The numerical solution at each step therefore amounts to solving a sparse linear system coupling bulk and interfacial unknowns.

We first eliminate the face fluxes $Q^{\alpha\pm}$ using the discrete constitutive relation Eq. (39), leaving $\Phi^{\omega\pm}$ and $\Phi^{\gamma\pm}$ as the remaining unknowns. Let the (diagonal) mass matrices be defined by

$$M^\pm := \frac{C^\pm}{\Delta t_n} V^\pm,$$

where V^\pm denotes the diagonal matrix of phase volumes $V_{i,j}^\pm$.

Let $\operatorname{div}^\alpha$ denote the full (bulk+interface) directional divergence operator used in Eq. (38) and let $\operatorname{grad}^{\alpha\omega}$ and $\operatorname{grad}^{\alpha\gamma}$ denote the bulk and interfacial contributions to the directional gradient. Since these operators are linear in their arguments, we introduce the linear operators

$$L^{\omega\omega,\pm} := - \sum_{\alpha \in \{1,2\}} \partial_Q (V^\pm \operatorname{div}^\alpha (B^{\alpha\pm}, \cdot)) K^{\alpha\pm} \partial_\Phi \operatorname{grad}^{\alpha\omega} (B^{\alpha\pm}, W^{\alpha\pm}, \cdot), \quad (42)$$

$$L^{\omega\gamma,\pm} := - \sum_{\alpha \in \{1,2\}} \partial_Q (V^\pm \operatorname{div}^\alpha (B^{\alpha\pm}, \cdot)) K^{\alpha\pm} \partial_\Phi \operatorname{grad}^{\alpha\gamma} (A^{\alpha\pm}, B^{\alpha\pm}, W^{\alpha\pm}, \cdot), \quad (43)$$

$$L^{\gamma\omega,\pm} := - \sum_{\alpha \in \{1,2\}} \partial_Q (V^\pm \operatorname{div}^{\alpha\gamma} (A^{\alpha\pm}, B^{\alpha\pm}, \cdot)) K^{\alpha\pm} \partial_\Phi \operatorname{grad}^{\alpha\omega} (B^{\alpha\pm}, W^{\alpha\pm}, \cdot), \quad (44)$$

$$L^{\gamma\gamma,\pm} := - \sum_{\alpha \in \{1,2\}} \partial_Q (V^\pm \operatorname{div}^{\alpha\gamma} (A^{\alpha\pm}, B^{\alpha\pm}, \cdot)) K^{\alpha\pm} \partial_\Phi \operatorname{grad}^{\alpha\gamma} (A^{\alpha\pm}, B^{\alpha\pm}, W^{\alpha\pm}, \cdot). \quad (45)$$

Equivalently, one may view these as Jacobians; here they are constant matrices.

The discrete system at a given time step can then be written as

$$\begin{aligned} & \left[\begin{array}{c|c|c|c} M^- + \theta L^{\omega\omega,-} & 0 & L^{\omega\gamma,-} & 0 \\ \hline 0 & M^+ + \theta L^{\omega\omega,+} & 0 & L^{\omega\gamma,+} \\ \hline -\theta L^{\gamma\omega,-} & \theta L^{\gamma\omega,+} & -L^{\gamma\gamma,-} & L^{\gamma\gamma,+} \\ 0 & 0 & -\lambda I & I \end{array} \right] \begin{bmatrix} \Phi_{n+1}^{\omega-} \\ \Phi_{n+1}^{\omega+} \\ \Phi_{n+\theta}^{\gamma} \\ \Phi_{n+\theta}^{\gamma+} \end{bmatrix} \\ &= \left[\begin{array}{c|c} M^- - (1-\theta)L^{\omega\omega,-} & 0 \\ 0 & M^+ - (1-\theta)L^{\omega\omega,+} \\ (1-\theta)L^{\gamma\omega,-} & -(1-\theta)L^{\gamma\omega,+} \\ 0 & 0 \end{array} \right] \begin{bmatrix} \Phi_n^{\omega-} \\ \Phi_n^{\omega+} \end{bmatrix} + \begin{bmatrix} V^- R_{n+\theta}^- \\ V^+ R_{n+\theta}^+ \\ 0 \\ F_{n+\theta} \end{bmatrix}. \quad (46) \end{aligned}$$

The horizontal and vertical separators highlight the arrow-type structure of the matrix, characteristic of domain-decomposition couplings between subdomain unknowns and interfacial unknowns.

Finally, for symmetric positive definite face-centered diffusion coefficients $K^{\alpha\pm}$, the operators $L^{\omega\omega,\pm}$ are symmetric positive definite on the active bulk unknowns. Moreover, under the standard finite-volume duality between divergence and gradient, the discrete adjoint relation also holds,

$$-L^{\gamma\omega,\pm} = (L^{\omega\gamma,\pm})^\top.$$

The resulting sparse linear system Eq. (46) is solved using an appropriate linear solver (direct or iterative), depending on problem size. A one-dimensional example is presented in App. C.

5 Numerical validation in static domains

We validate the accuracy and robustness of the proposed cut-cell formulation for static embedded geometries. Both single-phase and two-phase configurations are considered, for elliptic (steady diffusion) and parabolic (unsteady diffusion) problems. Analytical solutions and corresponding forcing terms used for verification are provided in each paragraph.

Let $\phi^{\text{ex}}(\mathbf{x}, t)$ denote the exact solution. Errors are evaluated from cell-averaged unknowns at selected times t_n (typically the final time), and reported separately over regular cells and cut cells. The index sets are defined by

$$\mathcal{I}_{\text{reg}} = \{(i, j) : \Gamma_{i,j} = \emptyset\}, \quad \mathcal{I}_{\text{cut}} = \{(i, j) : \Gamma_{i,j} \neq \emptyset\}, \quad \mathcal{I}_{\text{all}} = \mathcal{I}_{\text{reg}} \cup \mathcal{I}_{\text{cut}}.$$

For any subset $S \in \{\text{reg}, \text{cut}, \text{all}\}$, we define the discrete L^2 error norm as

$$\|e(t_n)\|_{2,S} = \left(\frac{\sum_{(i,j) \in \mathcal{I}_S} V_{i,j} |\Phi_{n,i,j}^\omega - \Phi_{n,i,j}^{\text{ex}}|^2}{\sum_{(i,j) \in \mathcal{I}_S} V_{i,j}} \right)^{1/2}, \quad (47)$$

where $\phi_{n,i,j}^{\text{ex}}$ denotes the exact solution evaluated consistently with the discrete unknown e.g. at the cell centroid for cell averages. We report

$$\|e\|_{2,\text{reg}}, \quad \|e\|_{2,\text{cut}}, \quad \|e\|_{2,\text{all}}.$$

The empirical convergence order is estimated between two successive grid resolutions h_i and h_{i+1} using

$$p_{2,S} = \frac{\log(\|e\|_{2,S}^{(i)} / \|e\|_{2,S}^{(i+1)})}{\log(h_i / h_{i+1})}, \quad S \in \{\text{reg}, \text{cut}, \text{all}\}. \quad (48)$$

In addition, a global convergence rate is computed as the least-squares slope of $\log(\|e\|_{2,S})$ versus $\log(h)$ over all considered grid resolutions.

5.1 Single-phase validation

We first assess the single-phase formulation in a static embedded geometry. The single-phase formulation is obtained by restricting the computation to the light phase Ω^- , i.e. by solving only for Φ^{ω^-} and Φ^{γ^-} and dropping all “+” variables and interfacial coupling equations. In the continuous setting, the embedded boundary $\Gamma = \partial\Omega^- \cap \Omega$ is equipped with the Robin condition

$$\mathbf{q}^- \cdot \mathbf{n} + \beta \phi^- = f \quad \text{on } \Gamma,$$

where \mathbf{n} is the outward unit normal to Ω^- . Integrating over a boundary segment $\Gamma_{i,j}$ gives

$$\int_{\Gamma_{i,j}} \mathbf{q}^- \cdot \mathbf{n} \, dS + \beta \int_{\Gamma_{i,j}} \phi^- \, dS = \int_{\Gamma_{i,j}} f \, dS.$$

Using the interfacial (cut) operator $\text{div}^{\alpha\gamma}$ to represent the boundary-flux contribution consistently with the bulk balance, the discrete Robin condition is enforced as

$$\sum_{\alpha=1}^d V_{i,j}^- \text{div}_{i,j}^{\alpha\gamma} (A^{\alpha-}, B^{\alpha-}, Q_{n+\theta}^{\alpha-}) + \beta \langle \Gamma_{i,j}, 1 \rangle \Phi_{n+\theta, i,j}^{\gamma-} = \langle \Gamma_{i,j}, 1 \rangle F_{n+\theta, i,j},$$

with the segment-averaged value $F_{n+\theta, i,j}$.

Dirichlet or Neumann boundary conditions are recovered in the limits $\beta \rightarrow \infty$ (with $f = \beta \phi_D$) and $\beta = 0$ respectively.

5.1.1 Johansen-Colella Problem 1: Star-shaped Poisson problem

We reproduce the classical embedded-boundary verification problem proposed by Johansen and Colella [13]. The physical domain Ω is star-shaped and defined in polar coordinates by

$$\Omega = \{(r, \theta) : 0 \leq r \leq R(\theta)\}, \quad R(\theta) = 0.30 + 0.15 \cos(6\theta). \quad (49)$$

We solve the Poisson equation

$$\Delta\phi = 7r^2 \cos(3\theta) \quad \text{in } \Omega, \quad (50)$$

supplemented with Dirichlet boundary conditions taken from the exact solution

$$\phi(r, \theta) = r^4 \cos(3\theta) \quad \text{on } \Gamma. \quad (51)$$

The right-hand side in Eq. (50) follows from the polar Laplacian identity $\Delta(r^m \cos(k\theta)) = (m^2 - k^2)r^{m-2} \cos(k\theta)$ with $m = 4$ and $k = 3$.

The problem is discretized on a uniform Cartesian grid of spacing h using the cut-cell operators of Sec. 4, with Γ embedded in the background mesh. Errors are reported using the L^2 norms defined in Eq. (47), distinguishing regular cells (fully inside Ω), cut cells (intersected by Γ) and all active cells.

h	$N_x = N_y$	N_Ω	$\ e\ _{2,\text{all}}$	$\ e\ _{2,\text{reg}}$	$\ e\ _{2,\text{cut}}$	p_{all}	p_{reg}	p_{cut}
0.0625	15	39	3.726e-3	1.236e-3	3.515e-3	-	-	-
0.03125	29	228	1.498e-3	1.067e-3	1.052e-3	1.31	0.21	1.74
0.015625	58	1138	3.098e-5	1.504e-5	2.708e-5	5.60	6.15	5.28
0.0078125	116	4868	1.139e-5	4.821e-6	1.032e-5	1.44	1.64	1.39
0.00390625	231	20166	3.958e-6	1.399e-6	3.703e-6	1.52	1.79	1.48
0.001953125	461	82018	1.327e-6	4.054e-7	1.264e-6	1.58	1.79	1.55
fit	-	-	-	-	-	2.41	2.52	2.37

Table 1: Johansen-Colella Problem 1: L^2 errors in regular, cut and all active cells and pairwise convergence orders. Here N_Ω denotes the number of active cells intersecting Ω (i.e. $V_{i,j}^- > 0$).

On the finest grids, the observed convergence rates stabilize around $p_{\text{all}} \approx 1.6$, with slightly higher rates in regular cells $p_{\text{reg}} \approx 1.8$ and comparable rates in cut cells $p_{\text{cut}} \approx 1.5$. The unusually large pairwise orders reported between some intermediate resolutions (e.g. $p \gtrsim 5$) reflect a clearly pre-asymptotic regime, in which the star-shaped boundary is still under-resolved (small N_Ω) and the error is dominated

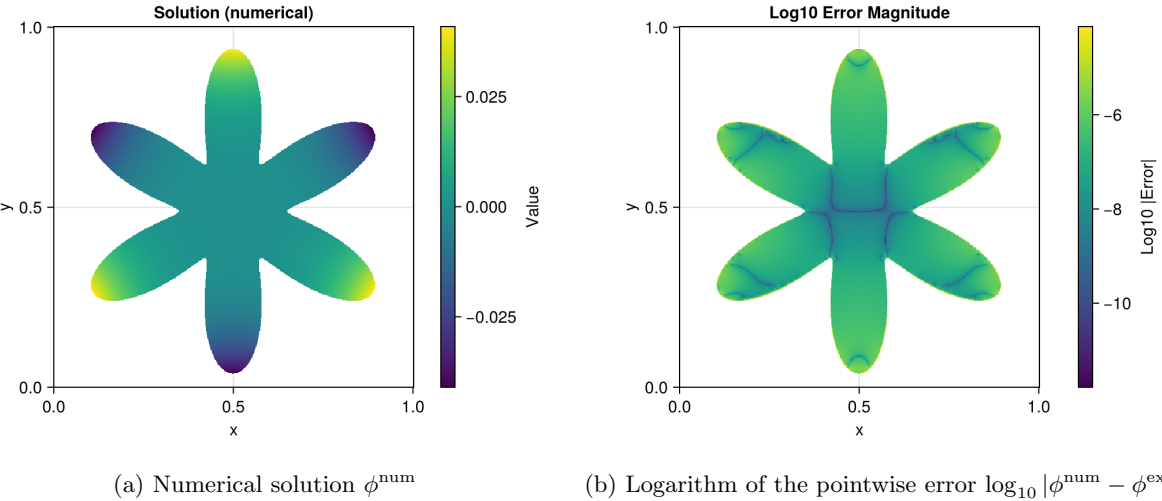


Figure 10: Johansen-Colella Problem 1 on the star-shaped domain Eq. (49): numerical solution and corresponding \log_{10} error field on a 512^2 mesh

by geometry-related effects and occasional favorable cancellations rather than the asymptotic truncation error.

This trend is consistent with the error fields shown in Fig. 10: the point-wise error concentrates near the embedded boundary and is larger in cut cells, while the interior region exhibits a smoother and smaller error distribution. As the grid is refined, the boundary layer of error contracts and the regular-cell contribution approaches the nominal second-order behavior, whereas the global rate remains slightly reduced due to the persistent influence of the cut-cell closure at the curved interface.

5.1.2 Johansen-Colella Problem 2: Flower-shaped steady diffusion (boundedness test).

As an additional boundedness/maximum-principle diagnostic, we reproduce a steady diffusion problem in the spirit of Johansen and Colella [13]. We consider a steady diffusion problem in the unit box with an embedded flower-shaped hole. The computational domain is the fixed Cartesian box $\Omega_{\text{box}} = [0, 1] \times [0, 1]$, from which a flower-shaped region is removed. The immersed boundary Γ is defined in polar coordinates (centered at $\mathbf{x}_c = (0.5, 0.5)$) by

$$r = R(\theta) = 0.25 + 0.05 \cos(6\theta), \quad (52)$$

and the physical domain is the exterior region

$$\Omega = \Omega_{\text{box}} \setminus \{(r, \theta) : 0 \leq r \leq R(\theta)\}.$$

We solve the Laplace equation

$$\Delta\phi = 0 \quad \text{in } \Omega, \quad (53)$$

with Dirichlet boundary conditions prescribed on both boundaries:

$$\phi = 1 \quad \text{on } \Gamma, \quad \phi = 0 \quad \text{on } \partial\Omega_{\text{box}}. \quad (54)$$

By the maximum principle, the exact solution is bounded within $[0, 1]$. We therefore monitor the discrete extrema $\min \phi^h$ and $\max \phi^h$ and the overshoot/undershoot ratio k/N , where k is the number of active cells with values outside $[0, 1]$ and N is the total number of active cells. No overshoot or undershoot is observed at any resolution, as summarized in Tab. 2. To stress the robustness of the proposed method, extremely coarse resolution are also considered here (only 4×4 cells).

5.1.3 Poisson equation in a disk with Robin boundary condition.

We next validate the single-phase formulation for an elliptic problem with a Robin boundary condition imposed on a curved embedded boundary. The computational box is $\Omega_{\text{box}} = [0, 4] \times [0, 4]$, and the physical domain is the disk

$$\Omega = \{(x, y) \in \Omega_{\text{box}} : (x - x_c)^2 + (y - y_c)^2 < R^2\}, \quad (x_c, y_c) = (2, 2), \quad R = 1.$$

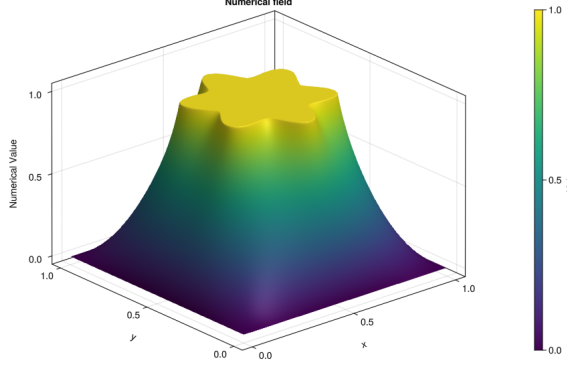


Figure 11: Johansen-Colella Problem 2: numerical steady diffusion field ϕ^{num} in the unit box, with the embedded flower-shaped boundary Eq. (52) defining a hole.

N_x	N_y	N_{cut}	N_{inside}	$\max \phi^h$	$\min \phi^h$	k/N
4	4	8	7	1.0	0.0	0.0
8	8	16	43	1.0	0.0	0.0
16	16	40	183	1.0	0.0	0.0
32	32	90	773	1.0	0.0	0.0
64	64	160	3195	1.0	0.0	0.0
128	128	328	12939	1.0	0.0	0.0
256	256	664	52099	1.0	0.0	0.0

Table 2: Johansen-Colella flower-shaped steady diffusion (boundedness test): discrete extrema and overshoot ratio k/N for increasing grid resolution. No violations of the physical bounds $[0, 1]$ are detected.

We solve the Poisson equation

$$-\Delta\phi = 1 \quad \text{in } \Omega, \quad (55)$$

supplemented with a Robin boundary condition on the embedded boundary $\Gamma = \partial\Omega$,

$$\partial_n\phi + \phi = 1 \quad \text{on } \Gamma, \quad (56)$$

where $\partial_n\phi = \nabla\phi \cdot \mathbf{n}$ and \mathbf{n} denotes the outward unit normal to Ω . The exact solution is

$$\phi^{\text{ex}}(x, y) = \frac{7}{4} - \frac{(x - x_c)^2 + (y - y_c)^2}{4}, \quad (57)$$

which satisfies $-\Delta\phi^{\text{ex}} = 1$ in Ω and the Robin condition Eq. (56) on Γ .

The discrete semi-norm H^1 error is defined from the gradient of the numerical solution,

$$\|e\|_{H^1, S} = \left(\frac{\sum_{(i,j) \in \mathcal{I}_S} V_{i,j} \|\nabla\Phi_{i,j} - \nabla\Phi_{i,j}^{\text{ex}}\|^2}{\sum_{(i,j) \in \mathcal{I}_S} V_{i,j}} \right)^{1/2},$$

where $\nabla\Phi$ is obtained with the discrete gradient operator of Sec. 4.1 and $\nabla\Phi^{\text{ex}}$ is evaluated at consistent locations. Pairwise orders are computed using Eq. (48). Tab. 3 reports the L^2 errors evaluated over all, regular and cut cells. Tab. 4 reports the H^1 semi-norm errors evaluated over all, regular and cut cells.

Tab. 3 confirms that the cut-cell formulation enforces the Robin condition on the curved embedded boundary with the expected accuracy. The L^2 error over regular cells converges at essentially second order once the mesh is sufficiently fine ($p_{2,\text{reg}} \approx 2$ for the last refinements), indicating that the scheme retains its nominal accuracy away from the boundary. Over all cells, the observed rate stabilizes around $p_{2,\text{all}} \approx 1.8$, reflecting the fact that the global error is influenced by the cut-cell region where geometric trimming and boundary closure dominate. The L^2 error restricted to cut cells converges slightly below

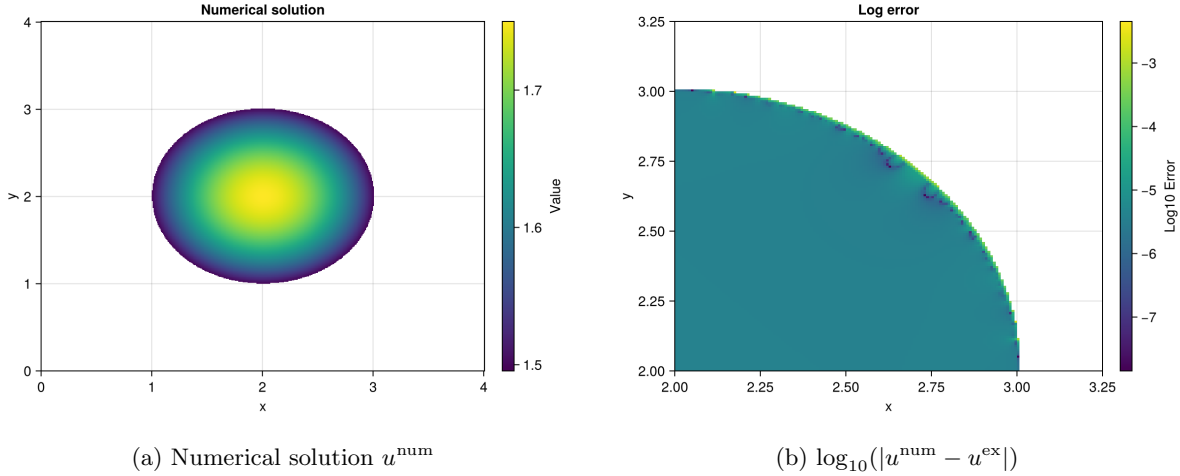


Figure 12: Poisson problem in a disk with Robin boundary condition Eq. (56): numerical solution and base-10 logarithm of the pointwise error.

h	$N_x=N_y$	$\ e\ _{2,\text{all}}$	$\ e\ _{2,\text{reg}}$	$\ e\ _{2,\text{cut}}$	$p_{2,\text{all}}$	$p_{2,\text{reg}}$	$p_{2,\text{cut}}$
0.25	8	$5.413e-3$	$3.883e-3$	$3.771e-3$	-	-	-
0.125	16	$1.216e-3$	$8.813e-4$	$8.382e-4$	2.15	2.14	2.17
0.0625	32	$4.198e-4$	$2.616e-4$	$3.284e-4$	1.53	1.75	1.35
0.03125	64	$1.209e-4$	$7.104e-5$	$9.788e-5$	1.80	1.88	1.75
0.015625	128	$3.476e-5$	$1.697e-5$	$3.033e-5$	1.80	2.07	1.69
0.0078125	256	$1.000e-5$	$4.056e-6$	$9.142e-6$	1.80	2.06	1.73
fit	-	-	-	-	1.79	1.96	1.70

Table 3: L^2 error convergence for the Poisson problem in a disk with Robin boundary condition, measured over all, regular, and cut cells.

h	$N_x=N_y$	$\ e\ _{H^1,\text{all}}$	$\ e\ _{H^1,\text{reg}}$	$\ e\ _{H^1,\text{cut}}$	$p_{H^1,\text{all}}$	$p_{H^1,\text{reg}}$	$p_{H^1,\text{cut}}$
0.25	8	$8.888e-2$	$7.618e-2$	$4.578e-2$	-	-	-
0.125	16	$4.456e-2$	$4.103e-2$	$1.738e-2$	1.00	0.89	1.40
0.0625	32	$2.290e-2$	$2.130e-2$	$8.419e-3$	0.96	0.95	1.05
0.03125	64	$1.181e-2$	$1.089e-2$	$4.550e-3$	0.96	0.97	0.89
0.015625	128	$5.797e-3$	$5.487e-3$	$1.871e-3$	1.03	0.99	1.28
0.0078125	256	$2.909e-3$	$2.763e-3$	$9.086e-4$	0.99	0.99	1.04
fit	-	-	-	-	0.98	0.96	1.11

Table 4: H^1 -semi-norm error convergence for the Poisson problem in a disk with Robin boundary condition, measured over all, regular, and cut cells.

second order ($p_{2,\text{cut}} \approx 1.7$ on the finest grids), which is consistent with the reduced regularity of the discrete operators near embedded boundaries. Finally, Tab. 4 shows that the discrete H^1 -semi-norm errors converge at first order, with overall slopes close to one ($p_{H^1,\text{reg}} \approx 1$, $p_{H^1,\text{all}} \approx 1$ and $p_{H^1,\text{cut}} \approx 1$), as expected for gradient reconstruction in the vicinity of irregular control volumes and curved boundary closures.

5.1.4 Unsteady diffusion in a sphere with Robin boundary condition (3D).

We finally consider a three-dimensional single-phase parabolic test in a spherical domain with a Robin boundary condition. The physical domain is the ball $\Omega = \{\mathbf{x} \in \mathbb{R}^3 : \|\mathbf{x}\| < R\}$, embedded in a fixed Cartesian box. Let $r = \|\mathbf{x}\|$. We solve

$$\partial_t \phi = a \Delta \phi \quad \text{in } \Omega, \quad (58)$$

with the radial Laplacian $\Delta\phi = \frac{1}{r^2} \frac{\partial}{\partial r} \left(r^2 \frac{\partial\phi}{\partial r} \right)$, and the Robin condition on $\Gamma = \partial\Omega$,

$$\left. \frac{\partial\phi}{\partial r} \right|_{r=R} + k\phi(R, t) = 0. \quad (59)$$

Starting from a uniform initial condition $\phi(\mathbf{x}, 0) = \phi_0$, an exact radial series solution is available [22]. The eigenvalues $\{\mu_n\}_{n \geq 1}$ satisfy

$$\mu_n \cot \mu_n + kR - 1 = 0, \quad (60)$$

and the solution reads

$$\phi(r, t) = \sum_{n=1}^{\infty} C_n \frac{\sin(\mu_n r / R)}{r} \exp(-a\mu_n^2 t / R^2), \quad (61)$$

with coefficients

$$C_n = \frac{2kR^2\phi_0}{\mu_n^2} \frac{\mu_n^2 + (kR - 1)^2}{\mu_n^2 + kR(kR - 1)} \sin(\mu_n). \quad (62)$$

Time integration is performed with the midpoint rule ($\theta = \frac{1}{2}$) up to $t_f = 0.1$, using the time step $\Delta t = 0.25 \min(\Delta x^2, \Delta y^2, \Delta z^2)$. We report L^2 errors at t_f over regular cells, cut cells and all active cells. For convenience, we also indicate N_{diam} , the number of grid points across the sphere diameter, to highlight that the method remains robust even on very coarse resolutions (down to $N_{\text{diam}} = 1$).

h	N_{diam}	$\ e(t_f)\ _{2,\text{reg}}$	$\ e(t_f)\ _{2,\text{cut}}$	$\ e(t_f)\ _{2,\text{all}}$	p_{reg}	p_{cut}	p_{all}
1.0	1	$3.149e-1$	$1.996e-1$	$3.729e-1$	-	-	-
0.5	3	$7.141e-2$	$1.362e-1$	$1.538e-1$	2.14	0.55	1.28
0.25	9	$3.582e-2$	$3.316e-2$	$4.881e-2$	1.00	2.04	1.66
0.125	14	$9.452e-3$	$5.780e-3$	$1.108e-2$	1.92	2.52	2.14
0.0625	34	$2.900e-3$	$1.303e-3$	$3.179e-3$	1.70	2.15	1.80
0.03125	70	$8.911e-4$	$3.201e-4$	$9.123e-4$	1.70	2.02	1.80
fit	-	-	-	-	1.82	2.07	1.85

Table 5: L^2 errors at final time $t_f = 0.1$ for the 3D single-phase unsteady diffusion problem in a sphere with Robin boundary condition.

Tab. 5 demonstrates that the proposed cut-cell framework extends to three dimensions: the geometric moments (trimmed volumes, face apertures and boundary measures) can be integrated robustly in 3D and lead to stable discretizations even on very coarse grids (e.g. $N_{\text{diam}} = 1$). On the finest refinements, the global error converges at approximately second order, with fitted rates $p_{\text{all}} \approx 1.9$ and $p_{\text{reg}} \approx 1.8$. The cut-cell error also exhibits near-second-order behavior ($p_{\text{cut}} \approx 2.0$), indicating that the Robin closure and the moment-based representation of the curved boundary remain accurate in three dimensions.

The non-monotone pairwise orders at coarse-to-intermediate resolutions (e.g. the low p_{cut} between $h = 1$ and $h = 0.5$, followed by larger rates) are symptomatic of a pre-asymptotic regime where the sphere is strongly under-resolved and the error is dominated by boundary closure effects. Once the diameter is resolved by a few tens of cells ($N_{\text{diam}} \gtrsim 30$), the rates stabilize and the expected asymptotic convergence is recovered.

Fig. 13 shows the radial profile of $\phi(\cdot, t_f)$ extracted along a line passing through the center. Blue markers denote the numerical solution sampled at cell centroids as a function of the radius $r = \|\mathbf{x}\|$, while the red marker highlights the discrete boundary value at $r = R$ (the cut-cell boundary/interfacial unknown used to impose Eq. (59)). The close agreement with the analytical radial series Eq. (61) confirms that the moment-weighted boundary closure remains accurate in 3D and that the boundary degree of freedom provides a consistent trace of the solution at Γ .

Neumann limit and global conservation. To verify global conservation in the pure Neumann limit, we set $\partial_n \phi = 0$ on Γ . The analytical configuration is chosen such that the domain-integrated quantity is constant in time. On the discrete level, we monitor the conserved integral and its relative drift,

$$I^h(t) = \sum_{\text{active cells } i} V_i \phi_i(t), \quad \delta I^h(t) = \frac{I^h(t) - I^h(0)}{I^h(0)}.$$

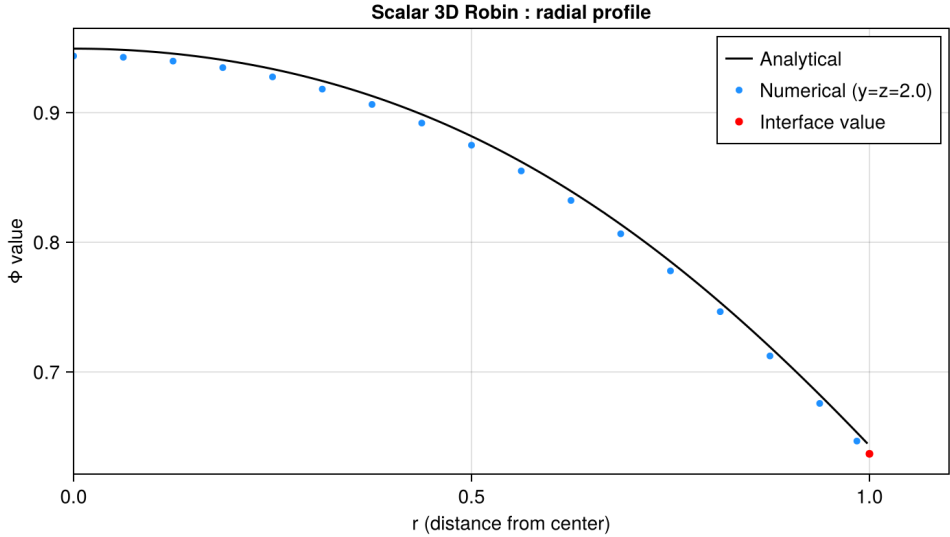


Figure 13: 3D unsteady diffusion in a sphere with Robin boundary condition: radial profile of $\phi(r, t_f)$ along a line through the center. Blue markers: numerical samples as a function of r . Red marker: discrete boundary/interfacial value at $r = R$ used in the Robin closure. Solid line: analytical series solution Eq. (61).

Using the same time-integration parameters as in the Robin tests (midpoint rule, $t_f = 0.1$), $I^h(t)$ remains constant up to machine precision: the maximum drift over $[0, t_f]$ is $|\delta I^h|_{\max} = 3.1 \times 10^{-17}$, and at the final time we obtain $\delta I^h(t_f) = 2.8 \times 10^{-17}$.

5.2 Two-phase validation

We now validate the two-phase formulation on several diffusion problem.

5.2.1 One-dimensional two-phase unsteady diffusion with homothetic jump

We consider a one-dimensional two-phase parabolic diffusion problem as a check of the jump enforcement in a minimal setting. The domain is the interval $\Omega = [0, L]$ split by a fixed interface at $x = x_{\text{int}}$ into

$$\Omega^- = \{x \in [0, L] : x < x_{\text{int}}\}, \quad \Omega^+ = \{x \in [0, L] : x > x_{\text{int}}\}, \quad (63)$$

where x_{int} is chosen so as not to coincide with a Cartesian face, so that the interface cuts a control volume.

In each phase we solve the unsteady diffusion equation with equal diffusivities $K^- = K^+ = K$,

$$\partial_t \phi^\pm = K \partial_{xx} \phi^\pm \quad \text{in } \Omega^\pm, \quad (64)$$

At the interface, we enforce continuity of diffusive flux together with a homothetic jump in the field:

$$[K \partial_x \phi] = 0, \quad \phi^+ - \lambda \phi^- = 0 \quad \text{at } x = x_{\text{int}}, \quad (65)$$

where λ is prescribed. A self-similar solution is obtained by introducing the similarity variables,

$$\eta^\pm(x, t) = \frac{x - x_{\text{int}}}{2\sqrt{Kt}},$$

and defining the constant

$$A = -\frac{\lambda}{1 + \lambda}. \quad (66)$$

The exact solution to the problem Eqs. (64)-(65) for all $t > 0$ is then given by

$$\phi^{-,ex}(x, t) = A \left[\text{erfc}(\eta^-(x, t)) - 2 \right], \quad x < x_{\text{int}}, \quad (67)$$

$$\phi^{+,ex}(x, t) = A \text{erfc}(\eta^+(x, t)) + 1, \quad x > x_{\text{int}}. \quad (68)$$

The outer boundary conditions are then prescribed as time-dependent Dirichlet condition taken from Eqs. (67)-(68):

$$\phi^-(0, t) = \phi^{-,\text{ex}}(0, t), \quad \phi^+(L, t) = \phi^{+,\text{ex}}(L, t),$$

and the initial condition too. In the results below, we take $\lambda = 100$ and $K^- = K^+$.

Tab. 6 reports L^2 errors at final time t_f over regular, cut and all active cells. Pairwise convergence orders are also provided.

λ	h	$\ e(t_f)\ _{2,\text{reg}}$	$\ e(t_f)\ _{2,\text{cut}}$	$\ e(t_f)\ _{2,\text{all}}$	p_{reg}	p_{cut}	p_{all}
100	2.0	$2.16e-1$	$2.90e-1$	$3.61e-1$	-	-	-
100	1.0	$1.85e-1$	$1.29e-1$	$2.25e-1$	0.22	1.17	0.68
100	0.5	$4.42e-2$	$3.62e-2$	$5.71e-2$	2.06	1.84	1.98
100	0.25	$2.74e-2$	$1.14e-3$	$2.74e-2$	0.69	4.99	1.06
100	0.125	$3.45e-3$	$1.21e-4$	$3.45e-3$	2.99	3.24	2.99
100	0.0625	$1.88e-3$	$2.44e-5$	$1.88e-3$	0.88	2.31	0.88
100	0.03125	$2.16e-4$	$9.07e-7$	$2.16e-4$	3.12	4.75	3.12
fit	-	-	-	-	2.00	3.53	2.00

Table 6: One-dimensional two-phase unsteady diffusion with homothetic jump $\lambda = 100$: L^2 errors at t_f over regular, cut and all cells, and corresponding convergence orders.

In addition to the stiff case $\lambda = 100$ reported below, we also consider a small sweep of homothetic jumps (e.g. $\lambda \in \{0.1, 1, 10, 100\}$) in order to visualize the interface enforcement. As λ varies, the analytical solution Eqs. (67)-(68) transitions from a weak to a strong discontinuity in ϕ across x_{int} , while the flux continuity constraint in Eq. (65) remains unchanged. This makes the test particularly sensitive to the discrete coupling: the method must simultaneously reproduce the prescribed jump amplitude and maintain consistent normal gradients on both sides of an interface that cuts a control volume.

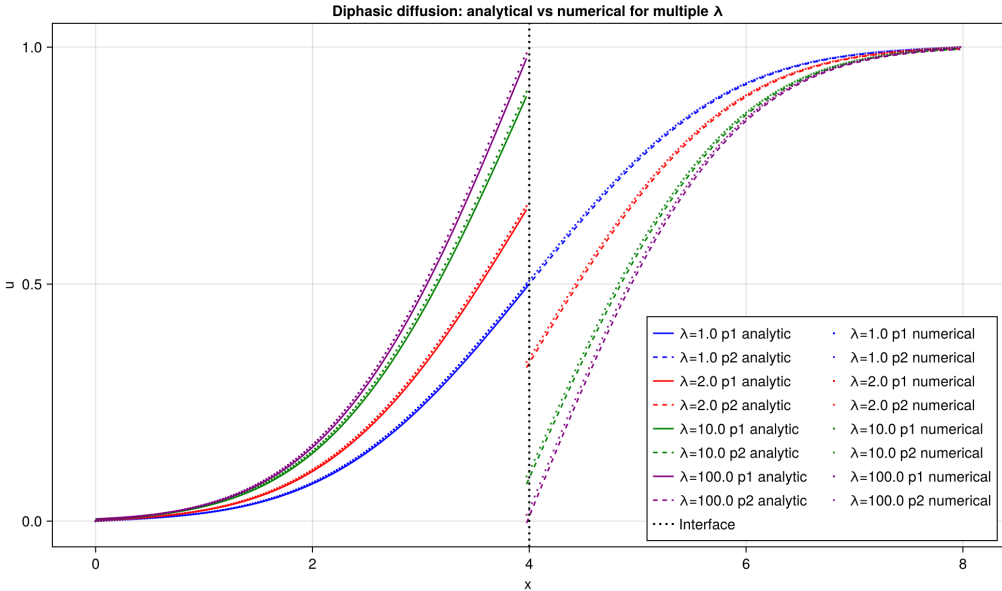


Figure 14: One-dimensional two-phase unsteady diffusion with homothetic jump: numerical solution (markers) and analytical profiles (lines) at the final time t_f for several jump ratios λ (e.g. $\lambda = 0.1, 1, 10, 100$). The vertical dashed line indicates the interface position x_{int} (chosen inside a cut cell: $x_{\text{int}} = 4.0 + 1e^{-2}$). The correct jump amplitude $\phi^+(x_{\text{int}}, t_f) = \lambda \phi^-(x_{\text{int}}, t_f)$ is recovered while preserving flux continuity across the interface.

For all λ values tested, the numerical profiles match the analytical solution near the interface and the discrepancy remains localized to a small neighborhood of the cut cell, confirming that the coupling is both sharp and stable even for large jump ratios.

5.2.2 Two-phase unsteady diffusion with a circular interface

The computational domain is the square cavity $\Omega = [0, L]^2$, $L = 8$, containing a circular interface Γ of radius $R_0 = 2$ centered at $\mathbf{x}_c = (4, 4)$. The phases are defined by

$$\Omega^+ = \{\mathbf{x} \in \Omega : r < R_0\}, \quad \Omega^- = \{\mathbf{x} \in \Omega : r > R_0\}, \quad r = \|\mathbf{x} - \mathbf{x}_c\|.$$

In each phase, we solve the unsteady diffusion equation with homogeneous Neumann conditions on the outer boundary $\partial\Omega$. At the interface, we consider the continuity case $\lambda = 1.0$, i.e. both the field and the normal diffusive flux are continuous across Γ . The initial data are chosen as $\phi^+(\mathbf{x}, 0) = \phi_0$ and $\phi^-(\mathbf{x}, 0) = 0$.

For this radially symmetric configuration, an analytical reference solution is available in polar coordinates (r, θ) in the form of integral representations involving Bessel functions. Denoting $K = \sqrt{K^+/K^-}$ and letting $\Phi(u)$ and $\Psi(u)$ be the auxiliary functions defined below, the solution reads

$$\phi^+(r, t) = \frac{4\phi_0 K^+ (K^-)^2}{\pi^2 R_0} \int_0^\infty e^{-K^+ u^2 t} \frac{J_0(u r) J_1(u R_0)}{u^2 [\Phi(u)^2 + \Psi(u)^2]} du, \quad (69)$$

$$\phi^-(r, t) = \frac{2\phi_0 K^+ \sqrt{K^-}}{\pi} \int_0^\infty e^{-K^+ u^2 t} \frac{J_1(u R_0) [J_0(K u r) \Phi(u) - Y_0(K u r) \Psi(u)]}{u [\Phi(u)^2 + \Psi(u)^2]} du, \quad (70)$$

and

$$\Phi(u) = K^+ \sqrt{K^-} J_1(R_0 u) Y_0(K R_0 u) - K^- \sqrt{D^+} J_0(R_0 u) Y_1(K R_0 u),$$

$$\Psi(u) = K^+ \sqrt{K^-} J_1(R_0 u) J_0(K R_0 u) - K^- \sqrt{D^+} J_0(R_0 u) J_1(K R_0 u).$$

Tab. 7 reports the L^2 errors at the final time t_f over regular cells, cut cells and all active cells in both phases. Several features are worth noting.

h	N_{diam}	$\ e(t_f)\ _{2, \text{reg}}$	$\ e(t_f)\ _{2, \text{cut}}$	$\ e(t_f)\ _{2, \text{all}}$	p_{reg}	p_{cut}	p_{all}
2.0	1	4.253e-1	5.620e-1	7.048e-1	-	-	-
1.0	2	2.363e-1	2.536e-1	3.467e-1	0.85	1.15	1.02
0.5	8	8.458e-2	4.781e-2	9.716e-2	1.48	2.41	1.84
0.25	12	4.358e-2	7.874e-3	4.429e-2	0.96	2.60	1.13
0.125	24	7.989e-3	1.190e-3	8.077e-3	2.45	2.73	2.45
0.0625	48	3.215e-3	2.951e-4	3.229e-3	1.31	2.01	1.32
fit	-	-	-	-	1.88	2.37	1.89

Table 7: L^2 error at final time t_f for the 2D two-phase diffusion test with a circular interface.

For the coarsest resolutions ($h = 2$ and $h = 1$), the circular interface is severely under-resolved and only a handful of cut cells represent the coupling between phases. Even though, the solver remains robust with at most 1 cell per domain diameter. Once the interface is resolved by $O(10)$ - $O(50)$ cells across the relevant length scale (here, from $h = 0.5$ down to $h = 0.0625$), the global error approaches a nearly second-order trend: the fitted rates are $p_{\text{all}} \approx 1.89$ and $p_{\text{reg}} \approx 1.88$. The global order is slightly below 2 because the solution remains influenced by the embedded interface region, where the local stencil is modified and the regular Cartesian cancellation is partially lost. Importantly, the convergence of the all-cells metric indicates that the two-fluid coupling does not spoil the accuracy of the bulk discretization. The cut-cell error decreases faster than the bulk error in this test, with a fitted rate $p_{\text{cut}} \approx 2.37$. This comparatively high rate is consistent with the fact that the coupling is enforced strongly through interfacial unknowns and moment-weighted operators, so that the dominant interface error can drop rapidly once smooth geometric under-resolution is removed. Some pairwise rates (e.g. the drop in p_{all} between $h = 0.5$ and $h = 0.25$) reflect the discrete change in the cut-cell topology as the interface position change relative to the background grid. As h changes, the set of cut cells and their aperture patterns are altered, which can temporarily bias the balance between bulk and interface contributions in the error norm. The convergence trend is nonetheless clear on the finest grids.

The temporal evolution of the interfacial diffusive flux provides an additional consistency check for the two-phase coupling. At each time step we evaluate

$$Q^+(t) = \int_{\Gamma} K^+ \nabla \phi^+ \cdot \mathbf{n} dS,$$

which measures the instantaneous transfer rate across the interface.

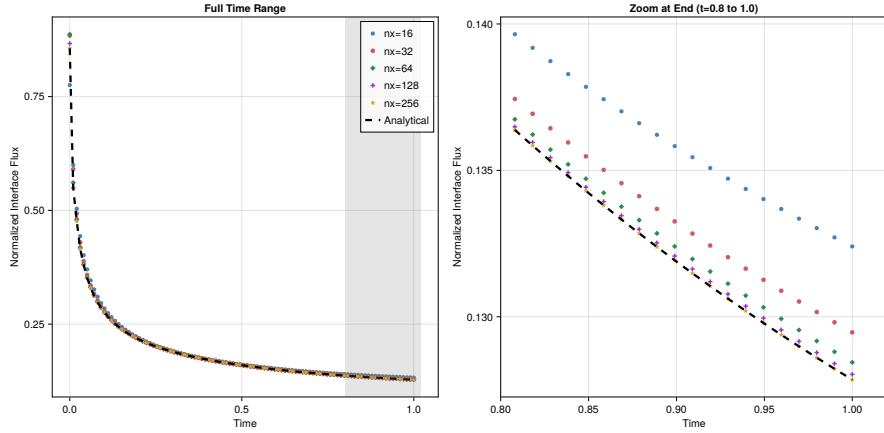


Figure 15: Two-phase unsteady diffusion with a circular interface: Normalized interfacial flux across the interface

The temporal evolution of the interfacial diffusive flux provides a stringent check of the two-phase coupling. Tab. 8 shows that the final flux value $Q^+(t_f)$ converges monotonically toward its reference value as the mesh is refined, with the relative error decreasing from 3.56×10^{-2} at $h = 0.5$ to 1.42×10^{-3} at $h = 0.0625$. The corresponding rates are close second order over this range, indicating that both the enforcement of the interfacial condition and the reconstruction of normal gradients in cut cells remain accurate. Fig. 15 further illustrates that the normalized interfacial flux history collapses under refinement: transient discrepancies on coarse grids diminish confirming that the method captures the time-dependent exchange across the embedded interface.

Resolution h	$Q^+(t_f)$	Relative error
0.5	0.1324020839	$3.560e-2$
0.25	0.1294676902	$1.265e-2$
0.125	0.1284444328	$4.642e-3$
0.0625	0.1280328469	$1.423e-3$

Table 8: Final interfacial flux diagnostic $Q^+(t_f)$ and relative error for the two-phase circular test.

5.2.3 Two-phase unsteady diffusion across a sphere

We conclude the validation with a three-dimensional two-phase test in a spherical geometry, for which a closed analytical reference is available in integral form [2]. This benchmark simultaneously checks the two-fluid coupling across a curved interface through scalar continuity and flux continuity and the robustness of the 3D moment integration required by the cut-cell discretization.

Let $\mathbf{x}_c = (2, 2, 2)$ and $R_0 = 1$. The interface is the sphere $\Gamma = \{\mathbf{x} : r = R_0\}$, $r = \|\mathbf{x} - \mathbf{x}_c\|$, splitting $\Omega_{\text{box}} = [0, 4]^3$ into the inner phase $\Omega^- = \{r < R_0\}$ and the outer phase $\Omega^+ = \{r > R_0\}$. We consider unsteady diffusion in the two phases Ω^\pm , with constant diffusivities D^- and D^+ . Across the interface Γ at $r = R_0$, we enforce continuity of the scalar field together with continuity of the normal diffusive flux.

The analytical solution corresponds to the classical configuration of an initially uniform inner concentration and vanishing outer concentration,

$$\phi^-(r, 0) = \phi_0, \quad 0 \leq r < R_0, \quad \phi^+(r, 0) = 0, \quad r > R_0, \quad (71)$$

together with decay at infinity, $\phi^+(r, t) \rightarrow 0$ as $r \rightarrow \infty$. In our bounded box, Dirichlet condition on $\partial\Omega_{\text{box}}$ are taken from the analytical solution evaluated at the boundary, so that the truncation does not pollute the error assessment.

The solution is radially symmetric, $\phi^\pm(\mathbf{x}, t) = \Phi^\pm(r, t)$. Following [2], we introduce the auxiliary parameters

$$\sigma = \sqrt{D^+/D^-}, \quad Q = \frac{D^+}{D^-} \sigma, \quad L = \frac{D^+ - D^-}{D^-}, \quad (72)$$

and the denominator

$$\mathcal{D}(u) = (u \cos u + L \sin u)^2 + (Q u \sin u)^2. \quad (73)$$

For the inner phase ($0 < r < R_0$), the exact solution reads

$$\Phi^-(r, t) = \frac{2Q\alpha\phi_0}{\pi r} \int_0^\infty \frac{(\sin u - u \cos u) \sin(ur/R_0)}{\mathcal{D}(u)} \exp(-D^- u^2 t/R_0^2) du. \quad (74)$$

For the outer phase ($r > R_0$), introduce

$$\mathcal{F}(u, r) = (u \cos u + L \sin u) \sin(u(r - R_0)/\sigma R_0) + Q u \sin u \cos(u(r - R_0)/\sigma R_0), \quad (75)$$

and the exact solution is

$$\Phi^+(r, t) = \frac{2\alpha\phi_0}{\pi r} \int_0^\infty \frac{(\sin u - u \cos u) \mathcal{F}(u, r)}{u \mathcal{D}(u)} \exp(-D^- u^2 t/R_0^2) du. \quad (76)$$

In practice, the integrals Eqs. (74)-(76) are evaluated by adaptive quadrature and truncated at a large cutoff. Time integration uses a midpoint time scheme, with a time step $\Delta t = 0.25 \min(\Delta x, \Delta y, \Delta z)$.

Tab. 9 reports the L^2 errors at the final time t_f over all active cells, regular cells and cut cells. The systematic decay of these three measures under mesh refinement confirms that the two-fluid two-phase coupling remains consistent in three dimensions. This benchmark is also a stringent stress test for the geometric layer: a spherical interface generates a broad spectrum of cut-cell patterns, including very small trimmed control volumes, strongly skewed face apertures and highly curved interface patches. The convergence observed in Tab. 9 therefore indicates that the three-dimensional moment integration (phase volumes, face apertures and interface measures/centroids) is sufficiently accurate and robust to sustain stable discrete flux balances and sharp enforcement of the interface conditions. The pairwise orders are not uniform across all refinement steps. For coarse meshes, the sphere is under-resolved and changes in cut-cell topology can temporarily shift the relative weight of bulk and interface contributions, leading to pre-asymptotic behavior. As the resolution increases, the regular- cell and global errors display a clear rapid decay, whereas the cut-cell error may exhibit apparent superconvergence.

h	N	$\ e(t_f)\ _{2,\text{all}}^{\text{rel}}$	$\ e(t_f)\ _{2,\text{reg}}^{\text{rel}}$	$\ e(t_f)\ _{2,\text{cut}}^{\text{rel}}$	p_{all}	p_{reg}	p_{cut}
0.5	4	4.845e-2	2.588e-2	4.096e-2	-	-	-
0.25	8	9.087e-3	8.116e-3	4.085e-3	2.41	1.67	3.33
0.12903226	16	2.748e-3	2.441e-3	1.261e-3	1.81	1.82	1.78
0.08333333	24	6.286e-4	6.251e-4	6.573e-5	3.37	3.12	6.76
0.04166667	48	1.771e-4	1.676e-4	2.167e-5	1.83	1.90	1.60
fit	-	-	-	-	2.28	2.07	3.13

Table 9: Two-phase unsteady diffusion in a sphere : L^2 errors at final time t_f over all, regular and cut cells, with pairwise convergence orders.

6 Conclusions and outlook

This work introduced a conservative Cartesian cut-cell finite-volume method for sharp-interface diffusion problems in static embedded geometries, in both single-phase and two-phase configurations. The formulation relies on a reduced geometric description: phase-restricted volumes, face apertures and a small set of low-order geometric moments that are sufficient to assemble compact stencils for discrete divergence and gradient operators. Boundary conditions (Dirichlet, Neumann and Robin) and interface jumps (normal diffusive flux and value) are enforced strongly in the algebraic system. A distinctive feature of the two-fluid approach is that interfacial unknowns are explicit degrees of freedom, providing direct access to interface values without post-processing or interpolation.

The numerical validation in static domains demonstrates accuracy, conservation, and robustness across a range of embedded geometries. Single-phase elliptic tests on non-convex domains recover near second-order convergence in L^2 norm, with cut-cell errors converging at comparable rates. The discrete solution remains within the expected physical range, with no overshoot or undershoot observed as the

grid is refined. For Robin boundary condition, the method maintains robust convergence in both L^2 and H^1 norms and preserves a faithful reconstruction of boundary unknowns. In three dimensions, the method extends without modification and remains effective even at very low resolutions, when the embedded body is represented by only a few cells. In the Neumann limit, the discrete mass is preserved to machine precision, highlighting exact flux conservation at the discrete level. Two-phase validations confirm that sharp coupling across interfaces does not compromise robustness or accuracy. The method exhibits near second-order convergence in global norms and appropriate behavior in cut cells, while the interfacial flux converges rapidly under refinement. Even with a strong homothetic jump, the coupling remains robust. Both the jump enforcement and the flux continuity remain well behaved as the interface cuts control volumes at arbitrary locations. Overall, the results show that the proposed method provides a reliable and geometrically flexible building block for interface-resolved diffusion with compact conservative operators constructed from a reduced set of moments, direct discrete enforcement of boundary and interface conditions, robust behavior in severely under-resolved regimes and consistent accuracy in both mono- and two-phase configurations.

While this article focuses on fixed interfaces, the formulation is designed as a foundation for more general sharp-interface models. Natural extensions include prescribed-motion geometries, free-boundary diffusion problems in which the interface motion is determined by interfacial balances, and Stefan-type phase-change models coupling diffusion to latent-heat conditions. Beyond pure diffusion, the same cut-cell machinery can be combined with sharp-interface incompressible flow solvers to address coupled advection-diffusion and two-phase transport. These developments will leverage the core properties established here ; local conservation, accurate interface coupling and robustness on complex embedded geometries, to tackle fully coupled multiphysics problems with dynamically evolving interfaces.

A Summary table for Static quantities notations

Quantity	Definition using $\langle \cdot, \cdot \rangle$	Equivalent integral form
Cell volume	$V_{i,j}^\pm(t) = \langle \Omega_{i,j}^\pm(t), 1 \rangle$	$\int_{\Omega_{i,j}^\pm(t)} 1 \, dV$
Cell centroid	$x_{i,j}^\pm(t) = \frac{\langle \Omega_{i,j}^\pm(t), x \rangle}{\langle \Omega_{i,j}^\pm(t), 1 \rangle}, \text{ eq for y}$	$\frac{\int_{\Omega_{i,j}^\pm(t)} x \, dV}{\int_{\Omega_{i,j}^\pm(t)} 1 \, dV}, \text{ eq for y}$
Face area (x-normal)	$A_{i-1/2,j}^{1\pm}(t) = \langle \Sigma_j^{1\pm}(t, x_{i-1/2}), 1 \rangle$	$\int_{\Sigma_j^{1\pm}(t, x_{i-1/2})} 1 \, dS$
Face area (y-normal)	$A_{i,j-1/2}^{2\pm}(t) = \langle \Sigma_i^{2\pm}(t, y_{j-1/2}), 1 \rangle$	$\int_{\Sigma_i^{2\pm}(t, y_{j-1/2})} 1 \, dS$
Centroidal face area (x-normal)	$B_{i,j}^{1\pm}(t) = \langle \Sigma_j^{1\pm}(t, x_{i,j}^\pm(t)), 1 \rangle$	$\int_{\Sigma_j^{1\pm}(t, x_{i,j}^\pm(t))} 1 \, dS$
Centroidal face area (y-normal)	$B_{i,j}^{2\pm}(t) = \langle \Sigma_i^{2\pm}(t, y_{i,j}^\pm(t)), 1 \rangle$	$\int_{\Sigma_i^{2\pm}(t, y_{i,j}^\pm(t))} 1 \, dS$
Staggered volume (x-direction)	$W_{i-1/2,j}^{1\pm}(t) = \langle \Omega_j^{1\pm}(t, [x_{i-1,j}^\pm, x_{i,j}^\pm]), 1 \rangle$	$\int_{\Omega_j^{1\pm}(t; [x_{i-1,j}^\pm, x_{i,j}^\pm])} 1 \, dV$
Staggered volume (y-direction)	$W_{i,j-1/2}^{2\pm}(t) = \langle \Omega_i^{2\pm}(t, [y_{i,j-1}^\pm, y_{i,j}^\pm]), 1 \rangle$	$\int_{\Omega_i^{2\pm}(t; [y_{i,j-1}^\pm, y_{i,j}^\pm])} 1 \, dV$
Bulk variable average	$\Phi_{i,j}^{\omega\pm}(t) = \frac{\langle \Omega_{i,j}^\pm(t), \phi^\pm(t) \rangle}{V_{i,j}^\pm(t)}$	$\frac{\int_{\Omega_{i,j}^\pm(t)} \phi^\pm(t) \, dV}{\int_{\Omega_{i,j}^\pm(t)} 1 \, dV}$
Interface variable average	$\Phi_{i,j}^{\gamma\pm}(t) = \frac{\langle \Gamma_{i,j}(t), \phi^\pm(t) \rangle}{\langle \Gamma_{i,j}(t), 1 \rangle}$	$\frac{\int_{\Gamma_{i,j}(t)} \phi^\pm(t) \, dS}{\int_{\Gamma_{i,j}(t)} 1 \, dS}$
Flux component (x-direction)	$Q_{i-1/2,j}^{1\pm}(t) = \frac{\langle \Sigma_j^{1\pm}(x_{i-1/2}), q^{1\pm}(t) \rangle}{A_{i-1/2,j}^{1\pm}}$	$\frac{\int_{\Sigma_j^{1\pm}(x_{i-1/2})} q^{1\pm}(t) \, dS}{\int_{\Sigma_j^{1\pm}(x_{i-1/2})} 1 \, dS}$
Source term average	$R_{i,j}^\pm(t) = \frac{\langle \Omega_{i,j}^\pm(t), r_{i,j}^\pm(t) \rangle}{V_{i,j}^\pm(t)}$	$\frac{\int_{\Omega_{i,j}^\pm(t)} r_{i,j}^\pm(t) \, dV}{\int_{\Omega_{i,j}^\pm(t)} 1 \, dV}$
Interface field average	$F_{i,j}(t) = \frac{\langle \Gamma_{i,j}(t), f(t) \rangle}{\langle \Gamma_{i,j}(t), 1 \rangle}$	$\frac{\int_{\Gamma_{i,j}(t)} f(t) \, dS}{\int_{\Gamma_{i,j}(t)} 1 \, dS}$

Table 10: Summary of geometric and semi-discrete quantities expressed using the generic integral notation $\langle \Xi, f \rangle$.

B Invertibility of the interfacial augmented system

We rewrite the 4×4 block system from 3 as

$$\underbrace{\begin{bmatrix} M^- + \theta L^{\omega\omega-} & 0 & L^{\omega\gamma-} & 0 \\ 0 & M^+ + \theta L^{\omega\omega+} & 0 & L^{\omega\gamma+} \\ -\theta L^{\gamma\omega-} & \theta L^{\gamma\omega+} & -L^{\gamma\gamma-} & L^{\gamma\gamma+} \\ 0 & 0 & -\lambda I & I \end{bmatrix}}_{\mathcal{M}} \begin{bmatrix} \Phi_{n+1}^{\omega-} \\ \Phi_{n+1}^{\omega+} \\ \Phi_{n+\theta}^{\gamma-} \\ \Phi_{n+\theta}^{\gamma+} \end{bmatrix} = \text{RHS.}$$

For compactness, set

$$\begin{aligned} A^- &:= M^- + \theta L^{\omega\omega-}, & A^+ &:= M^+ + \theta L^{\omega\omega+}, \\ C^- &:= L^{\omega\gamma-}, & C^+ &:= L^{\omega\gamma+}, \\ B^- &:= L^{\gamma\omega-}, & B^+ &:= L^{\gamma\omega+}, \\ D^- &:= L^{\gamma\gamma-}, & D^+ &:= L^{\gamma\gamma+}. \end{aligned}$$

Group bulk and interface unknowns as

$$\Phi^\omega := \begin{bmatrix} \Phi^{\omega-} \\ \Phi^{\omega+} \end{bmatrix}, \quad \Phi^\gamma := \begin{bmatrix} \Phi^{\gamma-} \\ \Phi^{\gamma+} \end{bmatrix}.$$

Then

$$\mathcal{M} = \begin{bmatrix} A & C \\ B & \widehat{D} \end{bmatrix}, \quad A = \text{diag}(A^-, A^+), \quad C = \begin{bmatrix} C^- & 0 \\ 0 & C^+ \end{bmatrix}, \quad B = \begin{bmatrix} -\theta B^- & \theta B^+ \\ 0 & 0 \end{bmatrix}, \quad \widehat{D} = \begin{bmatrix} -D^- & D^+ \\ -\lambda I & I \end{bmatrix}.$$

Standard assumptions leads to :

1. $M^\pm = \text{diag}(V^\pm/\Delta t) \succ 0$
2. (ii) $L^{\omega\omega\pm}$ and $L^{\gamma\gamma\pm}$ are symmetric positive definite (SPD) whenever the face diffusion tensors are SPD (jacobians of symetric divergence and gradient operators)

Hence A^\pm and A are SPD for any $\theta \in [0, 1]$. In the typical discrete adjoint setting, $B^\pm = (C^\pm)^\top$ and $D^\pm = (D^\pm)^\top$.

Eliminate Φ^γ via the Schur complement of the interface block:

$$S_\omega := A - C \widehat{D}^{-1} B.$$

The full system is invertible iff \widehat{D} and S_ω are both invertible, because $\det \mathcal{M} = \det \widehat{D} \cdot \det S_\omega$.

From the fourth row of \widehat{D} we have $\Phi^{\gamma+} = \lambda \Phi^{\gamma-}$. Substituting into the third row yields

$$(\lambda D^+ - D^-) \Phi^{\gamma-} + \theta B^+ \Phi^{\omega-} - \theta B^- \Phi^{\omega+} = 0.$$

Define the *effective interface operator*

$$D_{\text{eff}} := \lambda D^+ - D^-.$$

Then

$$\Phi^{\gamma-} = -\theta D_{\text{eff}}^{-1} (B^+ \Phi^{\omega-} - B^- \Phi^{\omega+}), \quad \Phi^{\gamma+} = \lambda \Phi^{\gamma-}.$$

Consequently, \widehat{D} is invertible iff D_{eff} is invertible. Since D^\pm are SPD,

$$D_{\text{eff}} = \lambda D^+ - D^- = (D^+)^{1/2} \left[\lambda I - (D^+)^{-1/2} D^- (D^+)^{-1/2} \right] (D^+)^{1/2}.$$

Thus $D_{\text{eff}} \succ 0$ whenever

$$\lambda > \lambda_\Gamma^{\max}, \quad \lambda_\Gamma^{\max} := \lambda_{\max}((D^+)^{-1/2} D^- (D^+)^{-1/2}).$$

Equivalently, for all $y \neq 0$, $y^\top D_{\text{eff}} y = \lambda y^\top D^+ y - y^\top D^- y \geq (\lambda - \lambda_\Gamma^{\max}) y^\top D^+ y$.

For invertibility of S_ω . Since $A^\pm \succ 0$, there exists $\alpha > 0$ such that

$$\langle x, Ax \rangle \geq \alpha \|x\|^2 \quad \forall x = \begin{bmatrix} x^- \\ x^+ \end{bmatrix}.$$

Moreover,

$$\|C D_{\text{eff}}^{-1} B\| \leq \|C\| \|D_{\text{eff}}^{-1}\| \|B\|.$$

Hence, if

$$\theta \|C\| \|D_{\text{eff}}^{-1}\| \|B\| < \alpha,$$

then for all $x \neq 0$,

$$\langle x, S_\omega x \rangle = \langle x, Ax \rangle - \theta \langle x, C \hat{D}^{-1} B x \rangle \geq (\alpha - \theta \|C\| \|D_{\text{eff}}^{-1}\| \|B\|) \|x\|^2 > 0,$$

Hence, S_ω is coercive and therefore invertible, since coercivity implies a trivial nullspace and a strictly positive Rayleigh quotient, i.e. all eigenvalues are positive and S_ω is SPD.

Remarks:

- For $\theta = 0$ (forward Euler), $S_\omega = A$ and is immediately invertible
- For $\theta > 0$, the mass terms in A^\pm increase α , enlarging the parameter window.

With $M^\pm \succ 0$ and $L^{\omega\omega\pm}, L^{\gamma\gamma\pm}$ are SPD then $D_{\text{eff}} := \lambda D^+ - D^-$ is SPD and the bulk-only Schur complement

$$S_\omega = \text{diag}(A^-, A^+) - \theta \begin{bmatrix} C^- \\ \lambda C^+ \end{bmatrix} D_{\text{eff}}^{-1} \begin{bmatrix} -B^- & B^+ \end{bmatrix}$$

is invertible. Consequently, the full matrix \mathcal{M} is invertible.

C One-dimensional two-phase diffusion problem

We consider three Cartesian cells of width Δx covering $x \in [0, 3\Delta x]$, with the middle cell cut by a sharp interface at $x_\Gamma \in (\Delta x, 2\Delta x)$. Denote $\ell^- = x_\Gamma - \Delta x$, $\ell^+ = 2\Delta x - x_\Gamma$, $\ell^- + \ell^+ = \Delta x$. At time level n we have four bulk averages Φ_1^n , $\Phi_2^{-,n}$, $\Phi_2^{+,n}$, Φ_3^n , and two interface-side values $\Phi_\Gamma^{-,n}$, $\Phi_\Gamma^{+,n}$.

Finite-volume balances With volumetric capacities C^- and C^+ and Backward Euler in time,

$$C^- \Delta x (\Phi_1^{n+1} - \Phi_1^n) = \Delta t (q_{3/2} - q_{1/2}), \quad (77)$$

$$C^- \ell^- (\Phi_2^{-,n+1} - \Phi_2^{-,n}) = \Delta t (q_\Gamma^- - q_{3/2}), \quad (78)$$

$$C^+ \ell^+ (\Phi_2^{+,n+1} - \Phi_2^{+,n}) = \Delta t (q_{5/2} - q_\Gamma^+), \quad (79)$$

$$C^+ \Delta x (\Phi_3^{n+1} - \Phi_3^n) = \Delta t (q_{7/2} - q_{5/2}). \quad (80)$$

Flux definitions Using midpoint-rule approximations,

$$q_{1/2} = a, \quad q_{3/2} = k^- \frac{\Phi_2^{-,n+1} - \Phi_1^{n+1}}{\frac{\Delta x}{2} + \ell^-}, \quad q_\Gamma^- = k^- \frac{\Phi_\Gamma^{-,n+1} - \Phi_2^{-,n+1}}{\ell^-},$$

$$q_\Gamma^+ = k^+ \frac{\Phi_2^{+,n+1} - \Phi_\Gamma^{+,n+1}}{\ell^+}, \quad q_{5/2} = k^+ \frac{\Phi_3^{n+1} - \Phi_2^{+,n+1}}{\ell^+ + \frac{\Delta x}{2}}, \quad q_{7/2} = b.$$

Interface conditions Continuity of the field and flux at x_Γ reads

$$\Phi_\Gamma^{-,n+1} - \Phi_\Gamma^{+,n+1} = 0, \quad q_\Gamma^- - q_\Gamma^+ = 0,$$

i.e.

$$k^- \frac{\Phi_\Gamma^- - \Phi_2^-}{\ell^-} = k^+ \frac{\Phi_2^+ - \Phi_\Gamma^+}{\ell^+}, \quad \Phi_\Gamma^- = \Phi_\Gamma^+.$$

Uniform-mesh limit If $\ell^- = \ell^+ = \frac{\Delta x}{2}$ and $k^- = k^+ = k$, then

$$q_{3/2} = \frac{k}{\Delta x} (\Phi_2^- - \Phi_1), \quad q_{5/2} = \frac{k}{\Delta x} (\Phi_3 - \Phi_2^+),$$

and (77)–(80) reduce to the standard second-order finite-volume scheme

$$C \Delta x (\Phi_i^{n+1} - \Phi_i^n) = \Delta t k \left[\frac{\Phi_{i+1}^{n+1} - \Phi_i^{n+1}}{\Delta x} - \frac{\Phi_i^{n+1} - \Phi_{i-1}^{n+1}}{\Delta x} \right],$$

demonstrating consistency.

Assembled linear system Collect the six unknowns at $n+1$ into

$$\Phi = [\Phi_1, \Phi_2^-, \Phi_2^+, \Phi_\Gamma^-, \Phi_\Gamma^+, \Phi_3]^T.$$

Define

$$\begin{aligned} m_1 &= C^- \Delta x, & m_2 &= C^- \ell^-, & m_3 &= C^+ \ell^+, & m_4 &= C^+ \Delta x, \\ \alpha_1 &= \frac{k^-}{\frac{\Delta x}{2} + \ell^-}, & \alpha_2 &= \frac{k^-}{\ell^-}, & \alpha_3 &= \frac{k^+}{\ell^+}, & \alpha_4 &= \frac{k^+}{\ell^+ + \frac{\Delta x}{2}}, \end{aligned}$$

and let $a = q_{1/2}$, $b = q_{7/2}$. Then the discrete system $\mathbf{A} \Phi = \mathbf{b}$ is

$$\mathbf{A} = \begin{pmatrix} m_1 + \Delta t \alpha_1 & -\Delta t \alpha_1 & 0 & 0 & 0 \\ -\Delta t \alpha_1 & m_2 + \Delta t(\alpha_1 + \alpha_2) & 0 & -\Delta t \alpha_2 & 0 \\ 0 & 0 & m_3 + \Delta t(\alpha_3 + \alpha_4) & 0 & -\Delta t \alpha_3 \\ 0 & 0 & 0 & 1 & -1 \\ 0 & -\alpha_2 & -\alpha_3 & \alpha_2 & \alpha_3 \\ 0 & 0 & -\Delta t \alpha_4 & 0 & 0 \end{pmatrix}, \quad \mathbf{b} = \begin{pmatrix} m_1 \Phi_1^n + \Delta t a \\ m_2 \Phi_2^{-,n} \\ m_3 \Phi_2^{+,n} \\ 0 \\ 0 \\ m_4 \Phi_3^n + \Delta t b \end{pmatrix}.$$

Rows 1-3 and 6 enforce the finite-volume balances (77)–(80), row 4 enforces $\Phi_\Gamma^- = \Phi_\Gamma^+$, and row 5 enforces $q_\Gamma^- = q_\Gamma^+$. This sparse system may be solved via a direct factorization or an iterative Krylov method with ILU preconditioning.

References

- [1] Robert Byron Bird, Warren E. Stewart, and Edwin N. Lightfoot. *Transport phenomena*. Wiley, New York, revised ed edition, 2007.
- [2] A Brown. Diffusion of Heat From a Sphere to a Surrounding Medium. *Australian Journal of Physics*, 18(5):483–490, October 1965.
- [3] Donna Calhoun and Randall J. LeVeque. A Cartesian Grid Finite-Volume Method for the Advection-Diffusion Equation in Irregular Geometries. *Journal of Computational Physics*, 157(1):143–180, January 2000.
- [4] Horatio S. Carslaw and J. C. Jaeger. *Conduction of heat in solids*. Clarendon Pr, Oxford, 2. ed., repr edition, 1980.
- [5] Yoann Cheny and Olivier Botella. The LS-STAG method: A new immersed boundary/level-set method for the computation of incompressible viscous flows in complex moving geometries with good conservation properties. *Journal of Computational Physics*, 229(4):1043–1076, February 2010.
- [6] A. Chierici, L. Chirco, V. Le Chenadec, R. Scardovelli, Ph. Yecko, and S. Zaleski. An optimized Vofi library to initialize the volume fraction field. *Computer Physics Communications*, 281:108506, December 2022.
- [7] E. L. Cussler. *Diffusion: Mass Transfer in Fluid Systems*. Cambridge University Press, 3 edition, January 2009.
- [8] James Gabbard and Wim M. Van Rees. A high-order finite difference method for moving immersed domain boundaries and material interfaces. *Journal of Computational Physics*, 507:112979, June 2024.
- [9] Frederic Gibou, Ronald P. Fedkiw, Li-Tien Cheng, and Myungjoo Kang. A Second-Order-Accurate Symmetric Discretization of the Poisson Equation on Irregular Domains. *Journal of Computational Physics*, 176(1):205–227, February 2002.
- [10] C.W Hirt, A.A Amsden, and J.L Cook. An arbitrary Lagrangian-Eulerian computing method for all flow speeds. *Journal of Computational Physics*, 14(3):227–253, March 1974.
- [11] C.W Hirt and B.D Nichols. Volume of fluid (VOF) method for the dynamics of free boundaries. *Journal of Computational Physics*, 39(1):201–225, January 1981.
- [12] M. Ishii and T. Hibiki. *Thermo-Fluid Dynamics of Two-Phase Flow*. Springer, New York, NY, 2011.
- [13] Hans Johansen and Phillip Colella. A Cartesian Grid Embedded Boundary Method for Poisson’s Equation on Irregular Domains. *Journal of Computational Physics*, 147(1):60–85, November 1998.
- [14] David H. Laidlaw, W. Benjamin Trumbore, and John F. Hughes. Constructive solid geometry for polyhedral objects. In *Proceedings of the 13th annual conference on Computer graphics and interactive techniques*, pages 161–170. ACM, August 1986.
- [15] Min Li, Hicham Chaouki, Jean-Loup Robert, Donald Ziegler, and Mario Fafard. Numerical Simulation of Stefan Problem Coupled with Mass Transport in a Binary System Through XFEM/Level Set Method. *Journal of Scientific Computing*, 78(1):145–166, January 2019.
- [16] A. Limare, S. Popinet, C. Josserand, Z. Xue, and A. Ghigo. A hybrid level-set / embedded boundary method applied to solidification-melt problems. *Journal of Computational Physics*, 474:111829, February 2023.
- [17] Peter McCorquodale and Phillip Colella. A high-order finite-volume method for conservation laws on locally refined grids. *Communications in Applied Mathematics and Computational Science*, 6(1):1–25, March 2011.
- [18] Brian Mirtich. Fast and Accurate Computation of Polyhedral Mass Properties. *Journal of Graphics Tools*, 1(2):31–50, January 1996.

- [19] Stanley Osher and James A Sethian. Fronts propagating with curvature-dependent speed: Algorithms based on Hamilton-Jacobi formulations. *Journal of Computational Physics*, 79(1):12–49, November 1988.
- [20] Charles S Peskin. Flow patterns around heart valves: A numerical method. *Journal of Computational Physics*, 10(2):252–271, October 1972.
- [21] Gerald L. Pollack. Kapitza Resistance. *Reviews of Modern Physics*, 41(1):48–81, January 1969.
- [22] Andrei D. Polyanin. *Handbook of Linear Partial Differential Equations for Engineers and Scientists*. Chapman and Hall/CRC, 0 edition, November 2001.
- [23] Stéphane Popinet. An accurate adaptive solver for surface-tension-driven interfacial flows. *Journal of Computational Physics*, 228(16):5838–5866, September 2009.
- [24] Ronald A Remmerswaal and Arthur E P Veldman. A sharp, structure preserving two-velocity model for two-phase flow. 2022.
- [25] Alejandro Quirós Rodríguez, Tomas Fullana, Vincent Le Chenadec, and Taraneh Sayadi. A Conservative Cartesian Cut Cell Method for the Solution of the Incompressible Navier-Stokes Equations on Staggered Meshes, 2022. Version Number: 1.
- [26] R. Sander. Compilation of Henry’s law constants (version 5.0.0) for water as solvent. *Atmospheric Chemistry and Physics*, 23(19):10901–12440, October 2023.
- [27] Sandro Santilli, Paul Ramsey, Daniel Baston, Mateusz Łoskot, Martin Davis, Regina Obe, Charlie Savage, Yury Bychkov, Even Rouault, and Michael Toews. GEOS (Geometry Engine, Open Source), November 2023.
- [28] R. I. Saye. High-Order Quadrature Methods for Implicitly Defined Surfaces and Volumes in Hyper-rectangles. *SIAM Journal on Scientific Computing*, 37(2):A993–A1019, January 2015.
- [29] Peter Schwartz, Michael Barad, Phillip Colella, and Terry Ligocki. A Cartesian grid embedded boundary method for the heat equation and Poisson’s equation in three dimensions. *Journal of Computational Physics*, 211(2):531–550, January 2006.
- [30] Roel Verstappen and Marc Dröge. A symmetry-preserving Cartesian grid method for computing a viscous flow past a circular cylinder. *Comptes Rendus. Mécanique*, 333(1):51–57, December 2004.
- [31] Roberto Verzicco. Immersed Boundary Methods: Historical Perspective and Future Outlook. *Annual Review of Fluid Mechanics*, 55(1):129–155, January 2023.